**The Thesis Committee for Claire Elisabeth Davis**
**Certifies that this is the approved version of the following thesis:**

# An Electrostatic Approach for Producing Nanoparticulate Membranes Using Laser Ablation of Microparticle Aerosols

**APPROVED BY**
**SUPERVISING COMMITTEE:**

**Supervisor:**

Desiderio Kovar

Michael F. Becker

# An Electrostatic Approach for Producing Nanoparticulate Membranes Using Laser Ablation of Microparticle Aerosols

**by**

**Claire Elisabeth Davis, BSE**

**Thesis**

Presented to the Faculty of the Graduate School of

The University of Texas at Austin

in Partial Fulfillment

of the Requirements

for the Degree of

**Master of Science in Engineering**

**The University of Texas at Austin**

**August 2011**

# Dedication

To my parents and my sisters.

A Mamette, qui continue à me guider dans mes choix et ma vie.

A Charlie, dont je partage maintenant l'amour des Etats-Unis.

# Acknowledgements

I probably learnt as much during my previous 23 years as during those two years in Austin, should it be in class, in the lab or on 6$^{th}$ street!

I discovered materials science, research and work on an American campus. For all of this, I would like to thank my supervisor, Dr Desiderio Kovar. His patience, guidance, support and advice enabled me to make this experience one of my own while staying on the right track. Dr Michael Becker and Dr John Keto are also to thank for their help, support and for sharing their knowledge and experience with me. I would further like to thank Kris Gleason for his enormous contribution to this work. His help in the lab and his insight in general were essential. Ralm Ricarte and Zachary Smith also greatly contributed to this thesis and working along with them has been easy and enjoyable. I am very grateful to Jack Clifford, Alan and Mike Ronalter for sharing some of their unbelievable skills. For their kindness and help in the lab, I want to thank Dr. Nathan Erickson and Dr. Kay Hoffman. For their patience, understanding and many interesting discussions, I thank Romain Fleury, Michael Gammage and Guillaume Noiseau.

I also learnt much more than just science and for that, I have many friends to thank. Jim Mikulak was a great office mate and a true guide as a TA. Ganesh Iyer and Mayur Mohan also made office life very enjoyable. Thank you to Sundeep Palvadi for bringing a smile to my face as often as he did. Gwennaël Beirnardt-Chartrel, Maria Benzekri, Erwan Chabert, Mathieu Leduc, Aurore Mercelat, Philippe Marouby and Elena

Nirlo were always there to share both my difficulties and my excitement at being on a different continent.

Finally, I would like to give special thanks to Manuj Nahar, for helping me with anything, supporting me at anytime, for many unforgettable moments, for making those two years such a human experience and most of all, for a friendship that I hope will live on for many, many more years.

# Abstract


## An Electrostatic Approach for Producing Nanoparticulate Membranes Using Laser Ablation of Microparticle Aerosols

Claire Elisabeth Davis, MSE

The University of Texas at Austin, 2011

Supervisor: Desiderio Kovar

The Laser Ablation of Microparticle Aerosols (LAMA) process produces nanoparticles by ablating microparticles that are entrained in an aerosol. Two of the main advantages of this process are that the particles produced are charged (preventing agglomeration) and bare (without a capping layer). Two different techniques are possible to collect the nanoparticles. In this work, the charged state of the particles formed was utilized to collect them electrostatically. This approach has the additional advantage that particles can be selected according to their size. The focus here was a particular application for gas separation. The nanoparticles produced were directly collected in a polymeric liquid, which was then irradiated with ultraviolet light to form a rubbery film. These membranes were tested for olefin/paraffin gas separation, a challenge that finds many applications, notably in the petroleum industry.

# Table of Contents

# List of Figures

# List of Tables

# Chapter 1: Introduction

The purpose of this Thesis is to present and discuss a method for producing nanoparticles via LAMA, collecting them electrostatically and incorporating them in a polymer membrane for use in a specific application.

### *Motivations for research*

Nanostructures have been subject to particular interest during the past decades. Due to their small size, they offer a range of new and unexpected properties and possibilities. In particular, they exhibit high surface-to-volume ratio which makes them more reactive than bulk material. An interesting aspect of nanomaterials is also the size-dependency of their properties. Many physical and chemical properties of materials (electrical, optical, magnetic, binding energy etc.) not only change from bulk to nanomaterial, but also become size-dependant in the small-size range. Since size is a tunable parameter (depending on the production technique), material properties can, in theory, be fine tuned to suit a particular application. This is of considerable interest, notably for catalytic purposes (1) but also in electronics (2) and in the medical field (3). The example of gold is very striking. As it scales down to the nano level, gold becomes magnetic, exhibits excellent catalytic activity, changes color and its melting temperature decreases drastically (4). In practice, although many processes have been developed to produce nanoscale particles, few techniques are able to produce large quantities of nanoparticles of a specific size with a very narrow-size distribution.

***Specific application: separation of olefins and paraffins***

One of the most direct applications for those particles is their use in selective membranes. In particular, separation of olefins and paraffins is one of the big challenges in the petrochemical industry. Light olefins (mostly ethylene and propylene) are widely used in a number of products from plastics to surfactants, styrene, Teflon, nylon, etc. The annual worldwide production of ethylene itself exceeds 75 million tons (5). They are produced by steam cracking of hydrocarbons from either naphta or natural gas. This process consists in breaking long alkane (paraffin) chains into unsaturated alkenes (olefins). Because alkanes are the most stable form of the constituent, this process does not produce a very high yield, resulting in a mixture of olefins and paraffins. The latter therefore need to be separated in order to isolate the desired olefin. As they have highly similar physical and chemical properties (boiling points for propylene and propane are 225K and 231K respectively (6)), this separation step is currently carried out in industry by fractional distillation which requires huge amounts of energy (annual energy used for cryogenic distillation of olefin/paraffin mixtures was estimated at $1.2 \times 10^{14}$ BTU (7)). Thus, separation technology that utilizes membranes for gas separation is of great technological interest as an alternative to the existing energy-intensive processes.

***Concept of selective membranes***

In concept, when a gas mixture is passed through an efficient selective membrane, the output flow should exhibit a much higher concentration in the desired gas than the

input flow. The two main parameters of a membrane are its selectivity and its permeability, always with respect to a specific gas or gas mixture. Permeability is described as the capacity of the membrane to let a specific gas go through during a permeation test. The permeability units and the method used to measure it are described in chapter IV of this Thesis. Selectivity is defined as the ratio of the permeability of the same membrane for two different gases, and thus describes the ability of the membrane to let one gas go through preferentially with respect to the other. Permeation can be divided into three steps. Sorption first takes place at the gas/membrane interface where the molecules of gas are adsorbed into the surface. Those molecules then diffuse through the membrane. In neat polymer membranes, diffusion can be described using Fick's laws and is the rate-limiting step of the process. In facilitated transport membranes, Fick's laws do not apply, as described in the following paragraph. Finally, desorption of the gas molecules at the opposite interface frees the gas from the polymer matrix.

***Facilitated transport membranes***

In conventional polymeric membranes, there is a tradeoff between permeability and selectivity meaning that if a membrane is very permeable for a gas, it will also be so for another, similar, gas and the selectivity of the membrane to the gas mixture will be low. To improve both permeability and selectivity, carriers which bond to a specific solute, can be added to the membrane. The carriers can act on either, or both, the diffusion step or the sorption step of permeation. Transport is facilitated through the

membrane as carriers bond with the adsorbed gas molecules, therefore enhancing permeability for this gas. It is important that any interaction between the carriers and the gas molecules be reversible in order for desorption to happen easily. Increased selectivity results from the selective bonding of carriers with a specific solute, so that transport is facilitated for only this gas.

Various types of matrices for facilitated transport membranes have been studied and attention has lately been focused on dry, solid rubbery polymers such as PEO (poly(ethylene oxide)) and PEGDA (poly(ethylene glycol) diacrylate) as they appear to be better suited for industrial applications than other existing membranes in terms of mechanical stability, practicality of preparation and use (8) (9).

In the case of olefin/paraffin separation and, in particular, in the cases of propylene/propane and ethylene/ethane separation, facilitated-transport membrane containing silver ions have widely been studied (10) (11) (12). Metal ions and olefins have the ability to form complexes as the olefin molecules donate electrons to the metal ions. The $\pi^*$ bond present in the olefin is involved in the chemical bonding to the ion as it offers a spare pair of electrons. As paraffins only have $\sigma$ bonds, the ions form complexes preferentially with olefins. The stability of those complexes varies with the type of metal ions (13). The complex formed by silver ions is relatively weak, enough for desorption to occur (14). Ag ions in rubbery polymer membranes have so far yielded very promising results for the separation of olefins and paraffins as they increase the selectivity of the membrane while keeping a reasonable permeability (8) (12) (15) (16) (17). However, the tradeoff between permeability and selectivity remains an issue, although it is already

greatly improved by the facilitated transport membranes with respect to the neat membranes. The mechanical stability of such membranes also remains a problem as they degrade relatively quickly over time (9) (12). This stems from the salt nature of the ions which are easily reduced or oxidized and subsequently lose their carrier properties. To avoid this problem, silver nanoparticles have recently been used in facilitated-transport membranes instead of silver ions, and have demonstrated good selectivity. It has been hypothesized that partial charges induced at their surface by suitable electron acceptors (such as ionic liquids) allow the nanoparticles to still display carrier properties and selectively facilitate the transport of olefins with respect to paraffins (18) (19) (20).

***Selectivity models***

To optimize the efficiency of such facilitated transport membranes, separation and binding models have recently been developed. A kinetic Monte-Carlo model of membranes (both neat and containing nanoparticles) show how control parameters affect the statistics of separation efficiency of membranes (21). Application of this model to Ag shows that there exist optimal conditions for separation efficiency. Diffusivity is decreased for olefin molecules that bind to nanoparticles because of the energy required for binding. Sorption of olefins, however, is enhanced by the presence of binding sites, whereas sorption of paraffins is decreased, therefore increasing the selectivity of the membrane. The optimal applied pressure is reached when the rate of olefin molecules entering the membrane corresponds to the rate of olefin molecules leaving a binding site.

At this optimal pressure, higher selectivity is obtained with weaker binding sites. The density of binding sites (and therefore of nanoparticles) in the membrane should also be increased to optimize selectivity.

Another theoretical study considers the binding energy of ethylene to various metals and alloys and investigates the influence of particle size on this binding energy in order to determine the most efficient parameters for ethylene/ethane separation (22). The binding sites that were considered include (111) faces, edge sites and corner sites. This study shows that Ag exhibits particularly low binding energy towards ethylene and therefore enhances weak chemisorption. The di-σ bonds to (111) faces, however, seems to be nonexistent in the case of Ag and should it exhibit a weak binding energy, it would surely enhance the separation efficiency of Ag greatly. A linear relationship between d-band center and binding energy is established for most metals – Ag, Au, Cu, Pd, Ni – with the exception of Pt, as shown in Fig. 1 below. As mentioned earlier, binding energy becomes size dependent at the nanoscale. Although this model suggests such a dependency, it also showed that the size of the clusters of atoms affects the binding energy much less than the nature of the binding site (which depends on the material). To activate a (111)-face bond of Ag and keep the defect bonds weak, Au-Ag alloys were shown to be the best option.

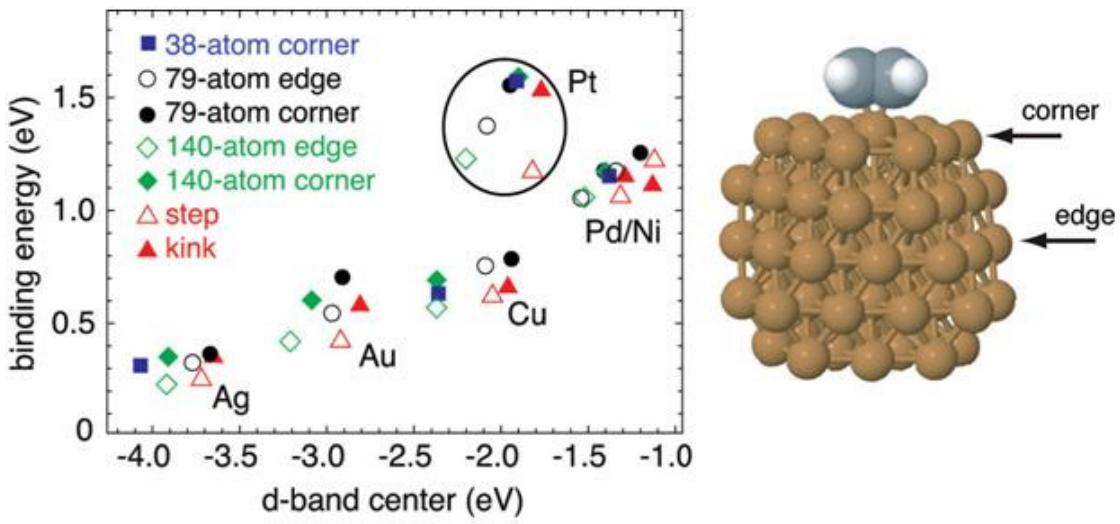


Figure 1. Correlation between the binding energy of ethylene at under-coordinated sites and the local d-band center, with the exception of Pt. Taken from (22)

***Existing methods for the production of metallic nanoparticles***

Many processes have already been developed to produce nanoparticles. Most chemical techniques use a bottom-up approach whereas physical techniques usually present a top-down method, each containing their own advantages and drawbacks.

In the synthesis of metallic nanoparticles, many involve the reduction of metal complexes in solution to form a colloidal dispersion. Others use electrochemical deposition routes. All eventually lead to nucleation and growth of metallic nanoparticles (23). One of the main and oldest chemical processes is the sol-gel process which uses hydrolysis and condensation reactions to produce a colloidal dispersion (24).

The physical methods include mechanical methods like milling or attrition. Some however are much more recent and complex, such as the Laser Ablation of Microparticle Aerosols (LAMA) presented in this thesis. Many physical methods (including the LAMA

process) offer the advantage of producing bare nanoparticles, i.e. not coated with an organic capping layer, and therefore directly reactive without further treatment.

The efficiency and relevance of a method is determined by its aptitude to control certain parameters such as particle shape, particle size, production efficiency (for eventual mass production), particle agglomeration and stability.

***Description of experimental objectives***

The aim of this project is to produce PEGDA membranes containing metal nanoparticles to be tested for ethylene/ethane and propylene/propane separation. The choice of materials used was based on the results presented in the Pozun-Henkelman model (22) as well as on time and cost considerations. It seemed to make sense to carry out the first tests and experiments on pure metals to determine the applicability of the Pozun-Henkelman model before going on to alloys. Silver was obviously the first choice as it is the most widely used metal for this application and is also predicted to offer superior properties according to the Pozun-Henkelman model. The second material tested was Au, as its binding energy to ethylene appears to be rather weak and close to that of Ag (given that their d-band centers are of the same order). Finally, Pd was chosen as the third material because of its closeness to Pt and its strong binding energy to ethylene. Indeed, we aim to investigate the extreme points in terms of binding energy in order to possibly observe a trend and relate to the theoretical study previously cited.

To produce such samples, the LAMA process was used in an electrostatic collection chamber. Both the process and the apparatus are described below.

# Chapter 2: *LAMA process*

***Description of the process***

The LAMA (Laser Ablation of Microparticle Aerosols) process, developed at the University of Texas at Austin (25) was used to produce nanoparticles for this study. To summarize the basic principles of the process, micron-sized particles that have the same composition that is intended for the nanoparticles are fed into a chamber via a gas flow to create an aerosol of microscale particles (of density $10^{-3}$ to $10^{-5}$ g/L). A laser beam is focused through the chamber and crosses the path of the aerosol flow. In the case of metallic microparticles, the laser beam strikes the front of a particle and is absorbed in a thin cross-section (with a thickness of order 10 nm) resulting in breakdown and the initiation of a shockwave, as shown in Fig. 2. Within the shockwave, the material is pressurized and heated above the critical point (26). The pressure and temperature in the material immediately adjacent to the shockwave is much lower than atmospheric pressure causing the vapor to condense extremely rapidly into nanoparticles. As the shockwave travels through the microparticle, the entire mass of the microparticle is converted into nanoparticles. When produced, the nanoparticles are positively charged due to thermionic emission and photo-ionization from the laser because the pulse length is longer than the time it takes the nanoparticles to condense. The nanoparticles stay in this state until they recombine with electrons present in the surrounding gas. As long as they are charged,

nanoparticles repel one another, therefore preventing agglomeration. One of the main advantages of this process is thus the ability to produce bare, single nanoparticles.

Nanoparticles as small as 1 nm have been demonstrated using the LAMA process but the mean size can be varied from about 2 - 40 nm (27). The size is determined by the growth and nucleation rates which are dependent on temperature, pressure, type of gas and material properties.

The produced nanoparticles can be collected in two different ways. In both cases, the particles are produced at about atmospheric pressure in a flowing gas. For the first method, the nanoparticles are accelerated through a small nozzle into the deposition chamber by a large pressure differential between the nanoparticle production and deposition chamber that is pumped by a vacuum (~100 mTorr). A substrate is placed directly beneath the nozzle at a distance that results in impaction of the nanoparticles onto the substrate surface (2 - 6 mm) at high velocities (28). A virtual impactor is placed in the ablation chamber, immediately after the ablation point. The microparticles and large nanoparticles remaining in the gas flow after ablation can be filtered out by this method. The geometry of the virtual impactor determines the cutoff size below which nanoparticles are collected.

The other collection technique is electrostatic collection. This method takes advantage of the charged state of the nanoparticles to deflect them with an electric field and collect them onto electrodes at much lower velocities than is possible by supersonic impaction. As the deflection path depends on the particle size and flow rate, it is in principle possible with this technique to collect non-agglomerated nanoparticles with a

very narrow size distribution (29). In practice, two electrodes are placed parallel to the flow direction. A positive voltage is applied to one electrode while the other is grounded. Positively charged particles will be deflected towards the grounded electrode. Any substrate making electrical contact with that electrode will therefore collect nanoparticles. This method only collects particles that remain charged until they make contact with the electrode. As will be discussed in section 3.4, recombination with the surrounding electrons happens fairly quickly after ablation. Therefore, the collection efficiency is rather low.

The technique used for experiments presented in this thesis is electrostatic collection.

Stage 1. Initial Breakdown

Laser 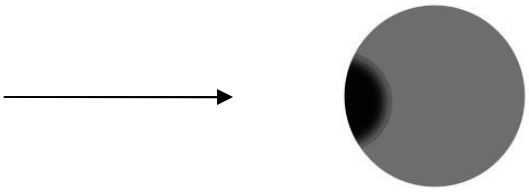

The laser pulse is absorbed at the front surface of metal particles.

Stage 2: Shockwave Formation

Laser-induced breakdown occurs at the front surface producing a shockwave, which travels through the particles.

Stage 3: Nucleation, Coalescence and Particle Charging

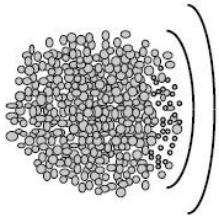

The vapor is rapidly quenched in the low pressure region behind the shockwave. The particles condense and are charged due to thermionic emission and photo ionization.

Figure 2. Laser ablation of a metal microparticle. Schematics taken from (43)

# Chapter 3: *Experimental procedures*

## 3.1 Optical setup

***Laser properties***

The laser used in this process is a Lumonics KrF excimer laser (model PM-848) filled with a mixture of KrF, Ne and He gases. It has a wavelength of 248 nm and the beam has a rectangular shape of dimensions 13 mm x 36 mm with a divergence angle of 6 mrad and can be pulsed at 200 Hz with a pulse length of about 12 ns. For these experiments, it was used at energy between 200 and 350 mJ.

The gas and particles flow in a vertical direction (z direction in Fig. 3) and the laser beam is in the x-direction. Therefore, the most stringent requirements on the beam size at the ablation spot are mainly in the y-direction, because the beam needs to be slightly wider than the particle flow (in order to ablate all particles) but as thin as possible in order to maximize the fluence. Thus, the width is determined by the nozzle width in the y-direction. The spot size in the z-direction has contradictory requirement since it is chosen to both maximize the fluence (small height) while maximizing the number of particles ablated (large height). From these considerations, the laser spot size is chosen to be 2 mm in width by 5 mm in height to obtain a laser fluence of 2 to 3.5 J/cm$^2$.

***Optical setup***

To shape the laser beam to these dimensions, a set of lenses are used as shown in Fig. 3. All lenses are fused silica coated to minimize reflections at a wavelength of 248 nm. L1 and L2 are identical rectangular, cylindrical convex lenses of focal length 100 cm. They focus the beam in the y-direction. L3 is a square, spherical convex lens that acts to focus the beam in all directions. Its focal length is 25 cm. L3 is therefore placed 25 cm in front of the ablation spot for an optimal focus in the z-direction. To obtain a 5 cm laser spot size in that direction, L3 is placed at a distance D3 = 23 cm. To achieve a spot size of 2 mm in the y-direction, L1 and L2 are placed at distances D1 = 53 cm and D2 = 35 cm.

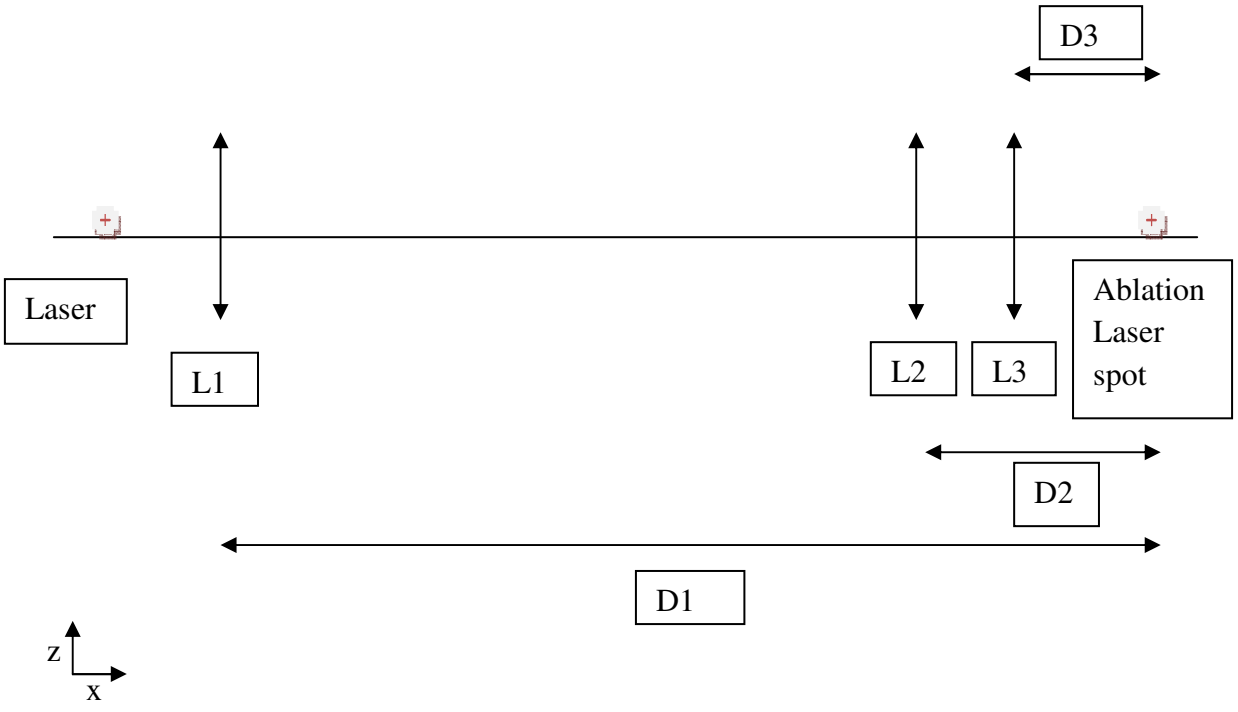


Figure 3. Schematic of optical setup

## 3.2 Chamber design and operation

The ablation chamber used to run the experiments is presented below. It is made up of several parts including the top part, the Teflon® tube and the bottom part, as shown in Fig. 4. The top and bottom parts are made out of stainless steel.

***Flow requirements***

The feedstock particles are carried through the whole chamber by the gas center flow. In order to maintain the laminarity of the particle flow, the center gas flow is surrounded by a coaxial gas flow that has the same velocity. The gas used for both center and coaxial flows is usually helium. The ideal velocity of the flows is determined by the laser spot size at the ablation point and the laser frequency. All the particles need to be struck by the laser at least once, but if particles are struck more than once, the nanoparticles produced from the first ablation will partially evaporate upon exposure to the beam the second time and be reduced in size, which can result in a broader nanoparticle size-distribution (30). However, it was observed experimentally that if the flows are set so that all the microparticles are hit by the laser twice and twice only, the resulting size-distribution is very narrow (as can be seen in the images chapter IV). As the laser spot length in the z-direction (gas flow direction) is 5 mm and the laser frequency is 200 Hz, the velocity of the gas (and therefore of the particles) should be 1 m/s for single ablation. The ideal center flow rate is then calculated from the volumetric flow rate using the nozzle area (0.06 x 0.145 $in^2$ = 5.61 $mm^2$) to be 340 sccm ($cm^3$/min)

for single ablation. The coaxial flow rate is calculated using the main cylinder area (3.77 $cm^2$) to be 22.59 L/min. In the case of double ablation, both flow rates need to be divided by a factor of two, so that the center flow rate becomes 170 sccm and the coaxial flow rate becomes 11.3 L/min. In all experiments presented below, the conditions for double ablation were chosen for two reasons: first to have the smallest possible particle sizes and size-distribution range while keeping a high enough production rate; second because the mass flow controllers used for the coaxial flow had a lower maximum flow rate than the rate required for single ablation.

***Description of the chamber***

Ablation of the microparticle aerosol takes place in the top part. The aerosol within the center flow is fed through a nozzle located at the top of the chamber. The laser beam needs to be exactly aligned with the particle flow below the nozzle. In order for the laser to pass through the chamber and ablate the particles in the flow, apertures are located on the main cylinder on either side of the ablation point. A fused silica window is placed at the end of a "horn" attached to each of these apertures. The purpose of horns is to prevent any damage to the window by increasing the distance from the windows to the ablation point; the beam is converging-diverging so the fluence at the location of the windows in the horns is much lower than at the ablation point. Care must be taken because, if some feedstock material deposits onto the windows, the latter may get solarized by the laser, absorbing significant amounts of the laser energy and significantly

heating up the stainless steel chamber. The horns also create stagnant gas regions next to the apertures which maintain the laminarity of the gas and particle flows as the aerosol passes the ablation point. Another, smaller horn is located in the negative y-direction in order to observe the ablation during experiments. A visible green discharge is an indication that ablation of Ag (or Pd) microparticles is occurring. For Au, the discharge is orange during ablation.

A teflon tube (25 cm long, 2.54 cm O.D.) fits into the top part. The two parts are sealed together using a quick disconnect fitting. Two apertures are cut out at the top of the teflon tube for the laser to pass through and are aligned with the top part with an insert into the main cylinder (it should be noted that if the Teflon tube is inserted into the top part too vigorously, it can push the insert up which results in misalignment and creates an opening that introduces turbulence in the flows). An acrylic window is also inserted at the top of the teflon tube and lines up with the quartz window in the top part, to enable the observation of the ablation. Two electrodes (stainless steel wires of diameter 0.032 in (0.81 mm)) are attached to the inside of the teflon tube by means of copper tape and scotch tape at the extremities of the tube (it should be noted that copper tape does not stick very well to Teflon and is only used on the ground electrode because, unlike scotch tape, it does not react with PEGDA). The electrodes are placed diametrically opposite to each other in the y-direction (perpendicular to the laser direction). One is connected to a positive voltage source (high voltage source adjustable from 0 to 2kV; for these experiments was kept at 500 V) while the other is grounded, thus creating an electric field

inside the Teflon tube in the y-direction. Positively charged nanoparticles are collected on the ground electrode.

At the bottom, the teflon tube fits into the bottom part using another quick disconnect fitting. The bottom part consists of two concentric cylinders. The inner cylinder passes the gas flow and any unablated feedstock material or other uncharged particles into a pipe connected to a fume hood. The purpose of the outer one depends on the type of collection used.

This chamber allows for two types of collection. The particles produced can be collected dry by placing a substrate (e.g. TEM grids) on the ground electrode. They can also be collected in a liquid (e.g. PEGDA to make polymer membranes) that is flowed on the ground electrode. This liquid is then collected in the outer cylinder of the bottom part. To increase the concentration of particles in the liquid, the liquid suspension is re-circulated through the chamber. For that purpose, a small stainless steel tube at the bottom of the outer cylinder of the bottom part is connected to a small stainless steel tube at the top of the top part. The latter is lined up with the ground electrode of the teflon tube (note that on Fig. 4, the liquid input tube on the top part has been rotated 90° for clarity and should actually be perpendicular to the laser beam direction). The connection between output and input liquid is made out of Tygon® LFL tubing L/S® 16, which is chemically resistant to PEGDA. A peristaltic pump (Masterflex L/S® Easy-Load® II model 77201-60) ensures the re-circulation of the liquid (between 1 and 600 rpm).

***Material choice***

Teflon was chosen as the material for the tube for several reasons. As it is connected to both electrodes as well as to the rest of the chamber, the tube needs to be electrically insulating to prevent a short-circuit between the two electrodes, as well as to prevent the entire stainless steel chamber from being charged, and to collect the particles only on one electrode. When used for liquid collection, the tube needs to be chemically inert to prevent any reaction with PEGDA, for example. It is also useful for the tube to be transparent in order to see the ablation point and the flow of particles. The initial material chosen was glass. However, when fitted to both the top and bottom parts, the glass tube was found to break easily due to the excessive mechanical constraint. Since Teflon is more flexible, it fits easily into the rest of the chamber, while being still rigid enough to keep the flows laminar. To compensate for the fact that the tube is not transparent, a window was cut at the top of the tube and teflon has been replaced by acrylic at this point in order to observe the ablation zone. The acrylic is not in contact with the PEGDA which flows on the opposite side of the tube. A tube made completely out of acrylic (which is transparent) can be used if collection is dry.

***Use of PEGDA inside the chamber***

The purpose of collecting directly in PEGDA is to facilitate the incorporation of the particles in a membrane in order to test its permeability and selectivity. Indeed, such a membrane can be made by adding a photo-initiator to the PEGDA and exposing it to UV

light. The polymer then cross-links, making a rubbery polymer membrane containing nanoparticles. The downside to using PEGDA directly in the ablation chamber, however, is that, when flowing close to the ablation point, the PEGDA is exposed to intense UV radiation and starts cross-linking inside the Teflon tube which results in the formation of solid polymer on the electrode and turbulence to the gas flows. To prevent this, a piece of aluminum shielding was attached inside the tube to protect the liquid flow from radiation from the laser. This shielding was painted black on the outside in order to render it insulating (in case it makes contact with the electrode) and to decrease light reflections (which also makes the ablation more visible).

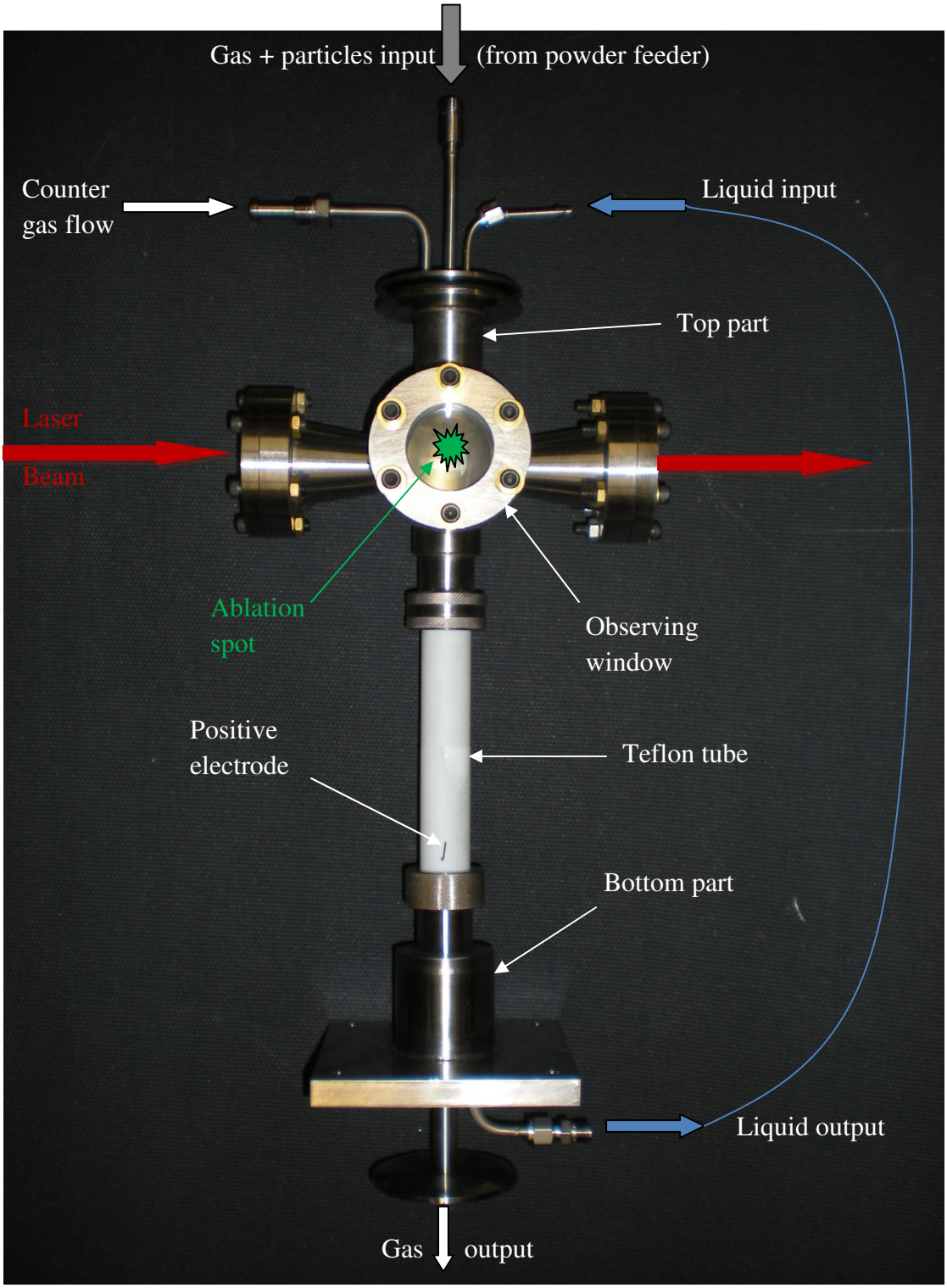


Figure 4. Picture of ablation chamber

***Chamber parameters***

There are several parameters that can be tuned in this chamber. Table 1 summarizes the values for the parameters that were kept constant through all the experiments presented later in this section. The parameters that varied are presented in the respective paragraphs where this work is discussed.

| **Laser fluence ($J/cm^2$)** | **Laser repetition rate (Hz)** | **Electrode voltage (V)** | **Type of gas** | **Nature of liquid** | **Number of laser pulses per particle** |
|---|---|---|---|---|---|
| 2 | 200 | 500 | He | PEGDA | 2 |

Table 1. Experimental parameters that were fixed for the experiments discussed in this thesis

## 3.3 Feeding System

The powder feeder that is used to produce the center-flow aerosol is made up of several parts, as described in Fig. 5. Each part has a specific purpose and some parts can be omitted depending on the context and objectives.

***General description of the feeding system***

The gas flow first passes through a needle valve (not shown on Fig. 5) that directs part of the flow to a rotameter. The other part of the flow is directed to the output flow of

a glass tube. The rotameter controls the flow to the aerosol generator and therefore controls the particle feed rate. The aerosol generator consists of a stainless steel cylinder containing a very small nozzle (~300 μm for the materials fed here). The feedstock powder is placed into the top part of the aerosol feeder. An eccentric motor (high-speed 9-18V DC motor from Radio Shack) is vibrated (the maximum speed attainable is 18000 RPM; during our experiments, the speed was lower). The vibration reduces the tendency for the powder to agglomerate or to stick to the walls of the aerosol feeder. Because it is accelerated through the small nozzle in the aerosol feeder, the gas flow containing the microparticles has enough momentum to rise up the glass tube and into the double virtual impactor. The larger diameter of the glass tube results in a first size selection on the microparticles, as the large ones that are too heavy to go all the way up the tube, fall back down instead. Another purpose of the glass tube is to break down or leave behind large agglomerates of particles that may have formed in the feedstock. The double virtual impactor (made out of aluminum, see Fig. 6) then results in a more thorough sorting of the particles, as detailed in a following paragraph. Using the needle valve placed before the aerosol feeder, it is possible to tune the flow going into the aerosol feeder and the glass tube without changing the total flow going into the double virtual impactor (which would modify its efficiency). Finally, the aerosol passes through a feed-rate sensor box to determine the aerosol particle density. Within this box, a second low-power cw laser (wavelength 635 nm, 5 mW maximum output power) is focused by a plano-convex lens (focal length 200 mm) and passed through the sensor box. The box is coated with black paint on the inside to reduce stray reflections and contains a photo detector at 90° to the

laser beam. The particles within the aerosol scatter the laser beam depending on their size, shape, and density. The signal from the photodetector is amplified using a custom designed amplifier and recorded using Labview® (National Instruments, Austin, TX). The particle size is computed using an algorithm that accounts for both absorption and scattering of the light by the particles (31) implemented using a Labview virtual instrument written by Kris Gleason and records the feed rate as a function of time. After passing the sensor, the aerosol flow then goes directly to the ablation chamber nozzle as indicated in Fig. 4.

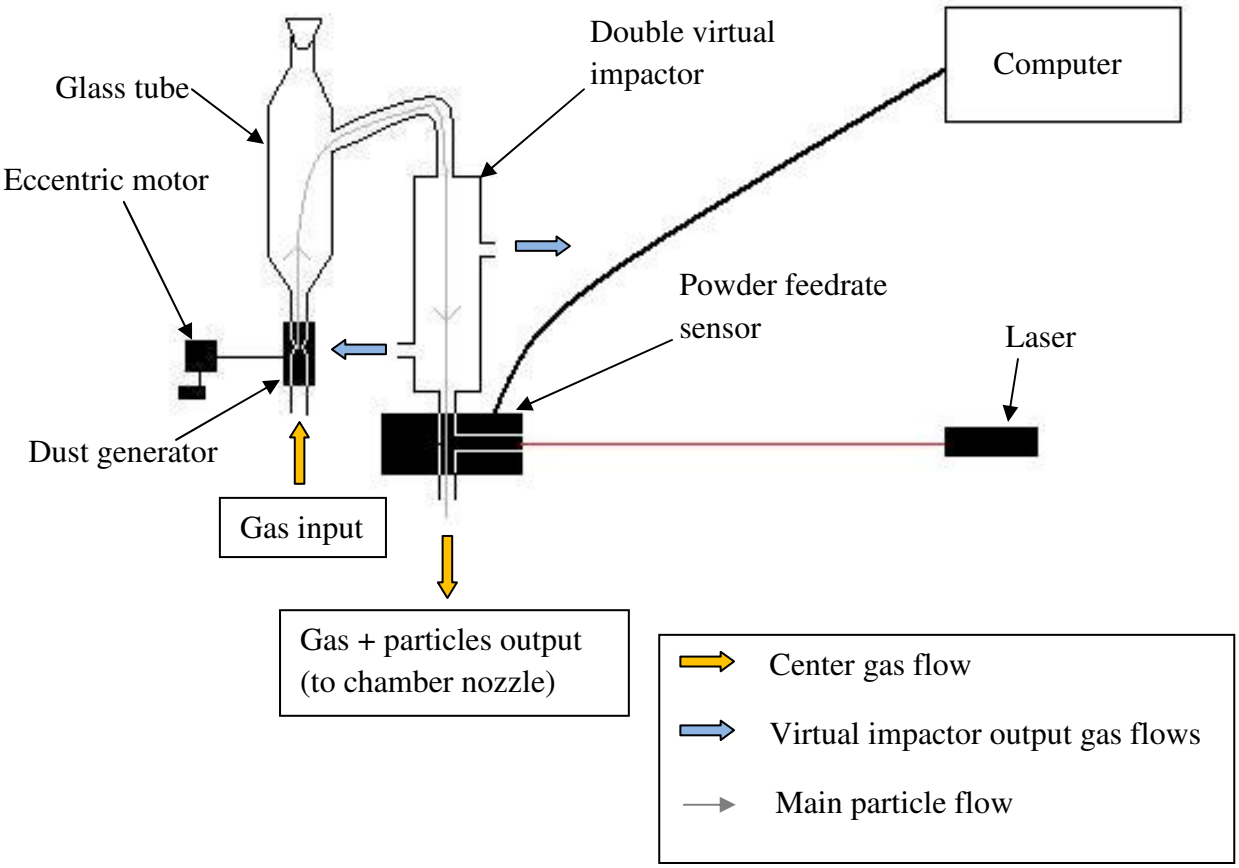


Figure 5. Schematic of powder feeding system

***Double virtual impactor calculations***

The double virtual impactor was designed based on the considerations outlined in a theoretical paper by Marple *et al.* (32) and experimental findings from papers by Chen *et al.* (33) (34). This design utilizes two consecutive virtual impactors, as shown on Fig. 6. The purpose of each virtual impactor (VI) is to filter microparticles according to their size by separating the aerosol flow (Q) into a major flow ($Q_M$ containing particles smaller than a given cutoff size) and a minor flow ($Q_m$ containing particles larger than the cutoff

size). Here, the top VI first removes the particles larger than cutoff size c1. The major flow from VI1 then becomes the aerosol flow to VI2 that removes particles smaller than cutoff size c2. In order to maintain an acceptable Reynolds number (if possible, larger than 1000), the aerosol flows for each VI need to be relatively high. However, the value for the center flow going into the chamber as determined by the dimensions of the chamber and the laser properties does not quite meet this requirement. Another purpose of VI2 is therefore to bridge the flow mismatch.

The cutoff size and efficiency of each VI depends on the dimensions of VI as well as the flows (see previously cited papers for more details). The Stokes number, *St*, is given by Fuchs (35):

$$St = \frac{\rho V C d^2}{9\mu w} \qquad \text{Equation \# 1}$$

where $\rho$ is the particle density, $V$ is the mean fluid velocity at the nozzle throat, $C$ is the Cunningham slip correction, $d$ is the particle diameter, $\mu$ is the absolute viscosity of the fluid and $w$ is the nozzle diameter.

The square root of the Stokes number can be considered a dimensionless particle size and can be plotted against collection efficiency in either minor or major flow. The cutpoint is given by $(St_{50})^{1/2}$, the value of $(St)^{1/2}$ at a 50% efficiency. For an ideal virtual impactor, 100% of particles with size corresponding to a higher $(St)^{1/2}$ than the cutpoint should be collected in the major flow. In reality, the curve is much more gradual. Nevertheless, $(St_{50})^{1/2}$ enables us to calculate the cutoff size of the virtual impactor, defined as the particle diameter $d_{50}$ corresponding to a 50% collection efficiency in both

the minor and major flow. Theoretically, 50% of the particles of diameter $d_{50}$ should go into each flow, but in reality, many particles will impact on the VI walls. References (32) (33) (34) present a number of theoretical and experimental plots showing the influence of several parameters on $(St_{50})^{1/2}$ and the relationship between $(St)^{1/2}$ and collection efficiency. This data was used to determine $(St_{50})^{1/2}$ and the calculation of the flows for the various experiments presented here.

To simplify the design of the impactor, the same VI geometry can be used for all the experiments by varying only the flows to adjust *St*. The nozzle diameter is thus fixed at $w_1$ = 0.111inch (0.282 cm) for VI1 and $w_2$ = 0.067 inch (0.170cm) for VI2. The cutoff size $d_{50}$ is determined by the size of the feedstock microparticles. $\rho$ is also determined by the feedstock material and $\mu$ depends on the type of gas used. The Cunningham slip correction depends on both the type of gas used and the particles fed according to the following equation (36):

$$C = 1 + \frac{2\lambda}{d}\left(A_1 + A_2 \exp\left(\frac{-A_3 d}{\lambda}\right)\right) \qquad \text{Equation \# 2}$$

where $d$ is the particle diameter, $\lambda$ is the mean free path of the gas and $A_1$, $A_2$, $A_3$ are constants that depend on the type of gas. For all the experiments presented, the gas used was helium. The values for helium were taken from (36) ($\lambda = 194.3\,nm \quad A_1 = 1.277 \quad A_2 = 0.370 \quad A_3 = 2.0$). The remaining parameter to calculate is $V$, which is used to determine the aerosol flow $Q$. The major flow ($Q_M$) and minor flow ($Q_m$) (see Fig. 6) are then calculated using the conservation of flows ($Q = Q_M + Q_m$) and the $\frac{Q_m}{Q}$ ratio determined by Chen *et al.* to optimize the sharpness of the collection efficiency curve and

to match the $(St_{50})^{1/2}$. The final value of the double VI output flow ($Q_{m2}$) is fixed by the center flow needed for the chamber (340 sccm for single ablation).

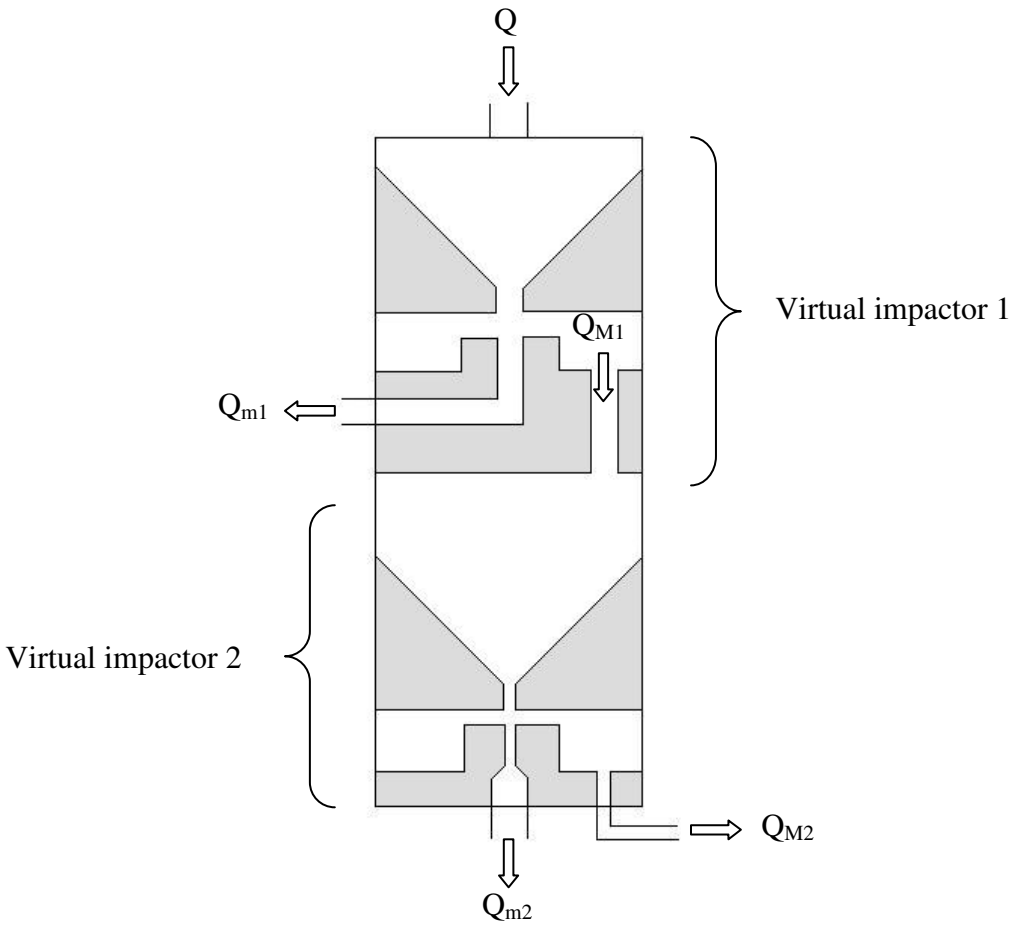


Figure 6. Schematic of double virtual impactor

***Reduced powder feeder***

The powder feeder used for all the presented experiments uses a setup slightly reduced from the one described above. The double virtual impactor was omitted because it did not appear necessary here. Indeed, the feedstock powders for all three materials used showed a narrow size-distribution of microparticles (as shown in SEM pictures in chapter IV) so that there was no need for size selection. Possible agglomerates or flocculates of microparticles were mostly broken up or filtered out in the glass tube. The feed rate sensor was also omitted for practical reasons as it was blocking out the flow of particles (this may have been caused by a leak). This, unfortunately, means that the feed rate is unknown throughout the experiments and compromises the feed rate comparisons between separate runs. However, the flow rate can still be controlled by the by-pass valve. Thus, the feed rate was controlled manually throughout each run.

## 3.4 Materials

Three different materials were used and compared in experiments. The materials were selected from the computational, density functional model of the interactions of olefin and paraffin gases with these materials described in Chapter I (22). Materials with a broad range of binding energies and binding sites were chosen in an attempt to characterize the influence of nanoparticles on membrane separation performance, as explained in Chapter I.

In addition to its uniqueness due to its weak binding energy, silver was selected as a baseline because it was used several years ago in a similar electrostatic chamber to make a membrane which significantly improved olefin/paraffin selectivity and permeation results compared to neat membranes. However, this was a single result with an unknown concentration of Ag and thus more experiments are needed to verify the validity of the data and the accuracy of the model. In addition, silver has since been used by the group for the making of membranes by impaction. Therefore, the first experiments were done using silver in order to compare results from this technique to others and to try and reproduce the initial encouraging result. The choice of Au and Pd as other materials to test was explained in Chapter 1.

### 3.4.1 Silver (basic experiment)

***Feedstock particles***

The silver powder was obtained from DuPont® (product P311L). As shown in Fig. 7 below, the average particle size is estimated to be 1.5 µm and the sizes ranged from 0.5 to 5 µm. The organic coating on the particles tends to cause agglomeration when in contact with moisture. The powder is hence kept in desiccators.

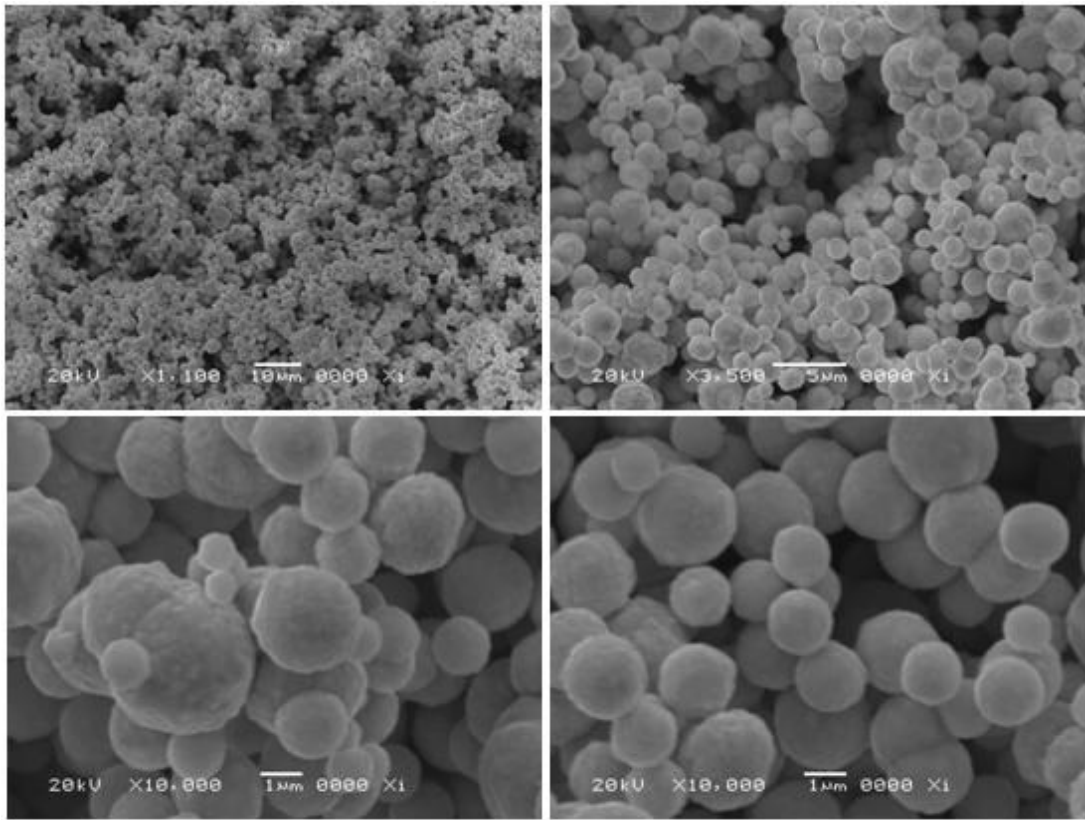


Figure 7. SEM micrographs of Ag feedstock

| Feedstock material | Duration (hrs) | Average feedstock particle diameter (μm) | Approximate volume of PEGDA re-circulated (mL) |
|---|---|---|---|
| Ag | 7 | 1.5 | 28 |

Table 2. Parameters specific to Ag

***Dry experiment with TEM grids***

This silver microparticulate powder was fed into the chamber and ablated dry (without PEGDA) for approximately 3 min. The nanoparticles were collected on lacey carbon TEM grids (883F from Ted Pella) at three positions in the Teflon tube: 1.5 cm, 9 cm and 16.5 cm down from the ablation point. The grids were kept on a ruler which lay on the ground electrode (therefore making electrical contact with it). The ruler was attached to the Teflon tube using magnets and scotch tape.

***Experiment with PEDGA***

The same powder was ablated for 7 hrs while about 28mL of PEGDA were flowed down the ground electrode and re-circulated. The experiment was carried out over one single day but the laser was run in increments of a maximum 2 hrs at a time in order to prevent the PEDGA from cross linking inside the tube and the apparatus from heating up too much.

The ablation was visible through the observation window and allowed for control over the stability of feed rate and laminarity of flows. Both remained relatively stable, with the exception of a few minutes following the addition of powder into the feeder. The ablation was then more intense and the flows seemed slightly more turbulent in the ablation region. Another rather striking observation is the change of color of the liquid throughout the experiment which was visible through the Tygon tubing used for recirculation. Neat PEGDA is initially transparent. After about 1.5 hrs of experiment, a

yellow tinge was visible in the liquid. After 2 hrs, its color had switched to darker yellow, almost grey. After that, the liquid kept getting darker until it was finally dark grey after 7 hrs of run. It should be noted that given the small diameter of the Tygon tubes, the color observed during the experiment seems much lighter than it would be in a larger vial. When transferred into a glass vial containing 30 mL, the final liquid appeared completely black. However, after leaving the vial to sit for 2 weeks, the liquid appeared completely transparent and black material was deposited at the bottom.

When the apparatus was dismantled right after the experiment, it was observed inside of the Teflon tube that some PEGDA had crosslinked right below the shielding and that some dark powder had stuck at certain points on the electrode (where the liquid had probably not covered the electrode at the end; it possibly changed path because the crosslinked polymer was in the way). Powder was also observed at the output point of the electrode (far down from the ablation point) which probably consisted mostly of large nanoparticles or even microparticles. Surprisingly, dark powder was also observed all along the positive electrode. Since it was not observed anywhere else in the tube, this suggests that it is not a turbulence problem but rather that some particles may be negatively charged when they form or become so very soon after ablation. The most likely scenario is that the positively charged particles recombine with surrounding electrons and become negatively charged via charge exchange with surrounding species.

In order to check whether the particles inside the PEGDA sample were in fact similar to those observed on the TEM grids, two samples were made by mixing respectively 1 drop of sample with 2 mL of ethanol (sample A) and 1 drop of sample with

5 mL of ethanol (sample B). The new mixes were thoroughly shaken and a drop of each was deposited on TEM grids (both lacey carbon and carbon Type B).

### 3.4.2 Gold

***Feedstock particles***

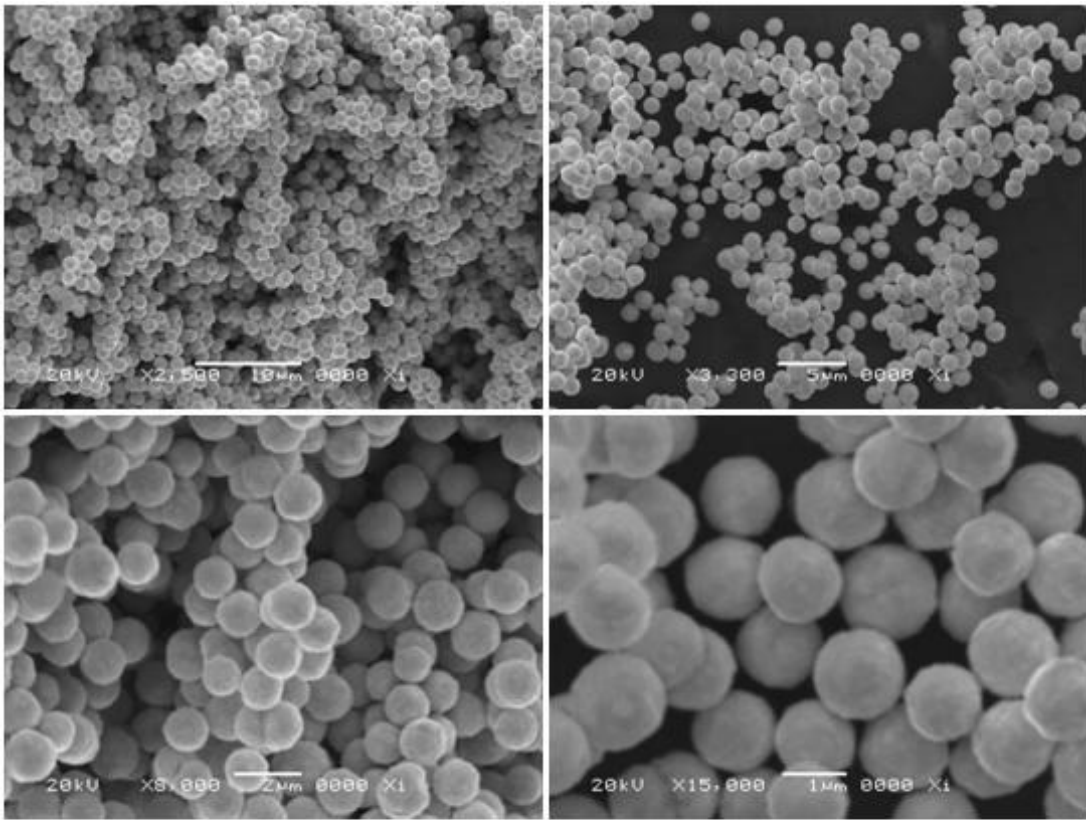


Figure 8. SEM micrographs of Au feedstock

The gold powder was obtained from DuPont® (product D100920-68). As shown in Fig. 8 above, the average particle size is estimated at 1.3 µm and sizes range from 1 to 1.5 µm. The Au particles seem to agglomerate much less than the Ag particles.

***Dry experiments with TEM grids***

This gold microparticulate powder was fed into the chamber and ablated in the same way as the equivalent Ag experiment. Nanoparticles were collected on lacey carbon TEM grids from Ted Pella placed 1.8, 4.3, 6.9 and 17 cm down from the ablation point (the shielding was also placed slightly lower than for the Ag experiment, so that the grid placed at 1.8 cm was right below the shielding). It should be noted that ablation was not as obvious as with Ag (as it does not exhibit the same green glow) but was still visible.

***Experiment with PEGDA***

| Feedstock material | Duration (hrs) | Average feedstock particle diameter (µm) | Approximate volume of PEGDA re-circulated (mL) |
|---|---|---|---|
| Au | 6.5 | 1.3 | 30 |

Table 3. Parameters specific to Au

The conditions of this experiment were mainly the same as the equivalent Ag experiment. An approximate volume of 30 mL of PEGDA was flowed down the ground electrode and re-circulated for 6.5 hrs. Ablation was less obvious than for Ag for the first few minutes of the experiments but was very clear afterwards. It seems that Au flows less easily than Ag and that it takes a few minutes for the He flows to carry the powder in a stable way.

For the remainder of this experiment except for a few minutes, the flows and the feed rate seemed very constant. In general, it can be noted that a higher feed rate seems to make the flows less laminar. After 4.5 hrs, the liquid appeared to have a blue tinge in the Tygon tubing. A 3 mL sample was taken out then. In the glass vial, the liquid exhibited a light but definite purple color. After 6.5 hrs, the remainder of the liquid (about 20 mL) was taken out and exhibited a slightly darker purple color when placed in the glass vial.

When the apparatus was dismantled right after the experiment, it was observed that some PEGDA had cross linked on the electrode below the shielding (more so than in the equivalent Ag experiment). This polymer exhibited a dark blue color. Some powder was also deposited around the output point of the electrode (far down from the ablation point) which exhibited a definite red color. The purple color of the liquid sample likely results from a mixture of small blue nanoparticles and larger red nanoparticles or even microparticles. It should be noted though that the color of the crosslinked polymer had changed to purple after being left for 2 weeks. Again, some particles were observed all along the positive electrode.

### 3.4.5 Palladium

***Feedstock particles***

The palladium powder was obtained from Technic Inc. (product 11-432, batch # 1584-2). As shown in Fig. 9 below, the average particle size is 0.5 µm (specification given by Technic Inc.) and the sizes range from 0.3 to 0.8 µm (estimated).

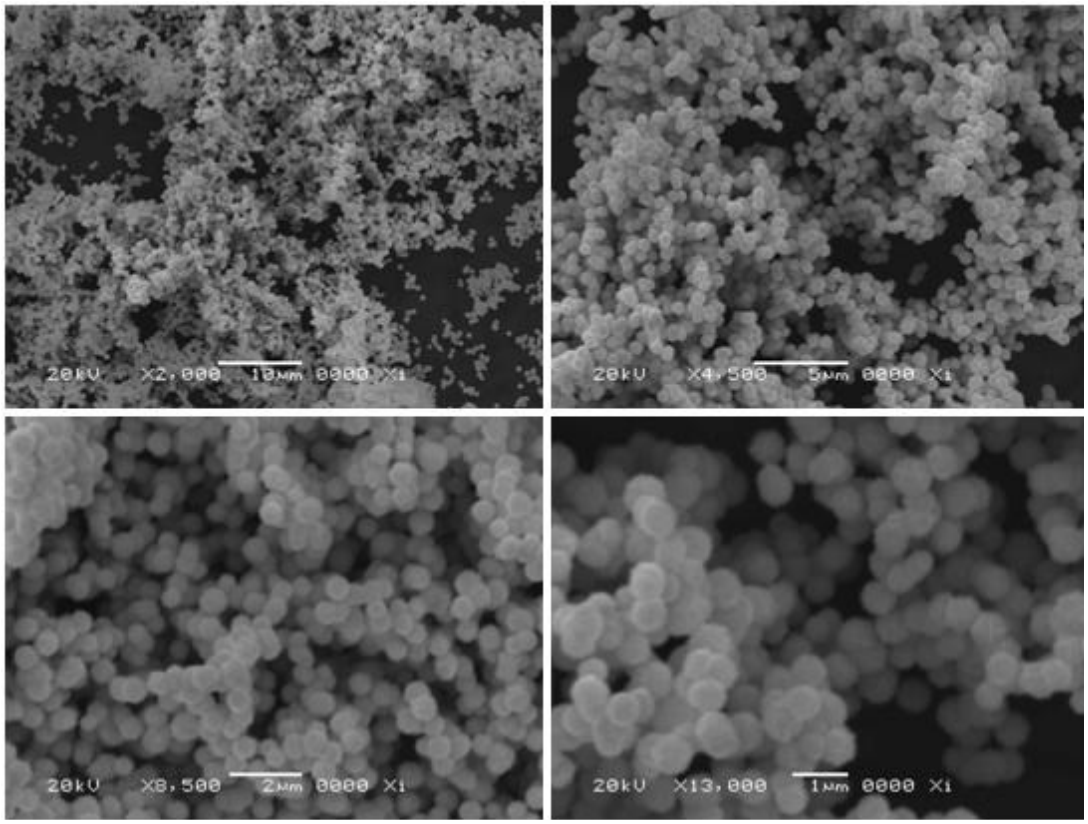


Figure 9. SEM micrographs of Pd feedstock

***Dry experiment with TEM grids***

The palladium microparticulate powder from Technic was fed into the chamber and ablated dry for 3 min. The nanoparticles were collected on lacey carbon TEM grids at four positions in the Teflon tube: 1.5 cm, 4 cm, 9 cm and 16.5 cm down from the ablation point. It was observed that the powder tended to get stuck in the feeder which needed to be gently tapped regularly in order to keep the powder flowing. This resulted in the feed rate not being very constant throughout an experiment.

In order to investigate the previous observation made during the Ag and Au experiments that some material was collected on the positive electrode, another set of TEM grids were kept on this positive electrode when Pd was ablated. The experiment was carried out in the same conditions with a collection time of 10 min instead of 3 min, as less material was expected to reach this electrode. The grids were placed at 1.3 and 6.3 cm down from the ablation point. Surprisingly, a very large amount of material was collected. EDS analysis should be carried out on this material to confirm that it is indeed Pd. As shown in Figs. 10-11, the particles are much agglomerated on both grids. On the grid placed further from the ablation point, the density is a little lower and the agglomerates are mostly larger, connecting into chains. It can be hypothesized that those particles agglomerated after recombining with surrounding electrons. Those agglomerates may then have gained their negative charge by combination with surrounding electrons or charge exchange with other negatively charged species. This would then correlate with the fact that particles collected with the supersonic impaction technique are much more agglomerated than particles collected with the electrostatic technique.

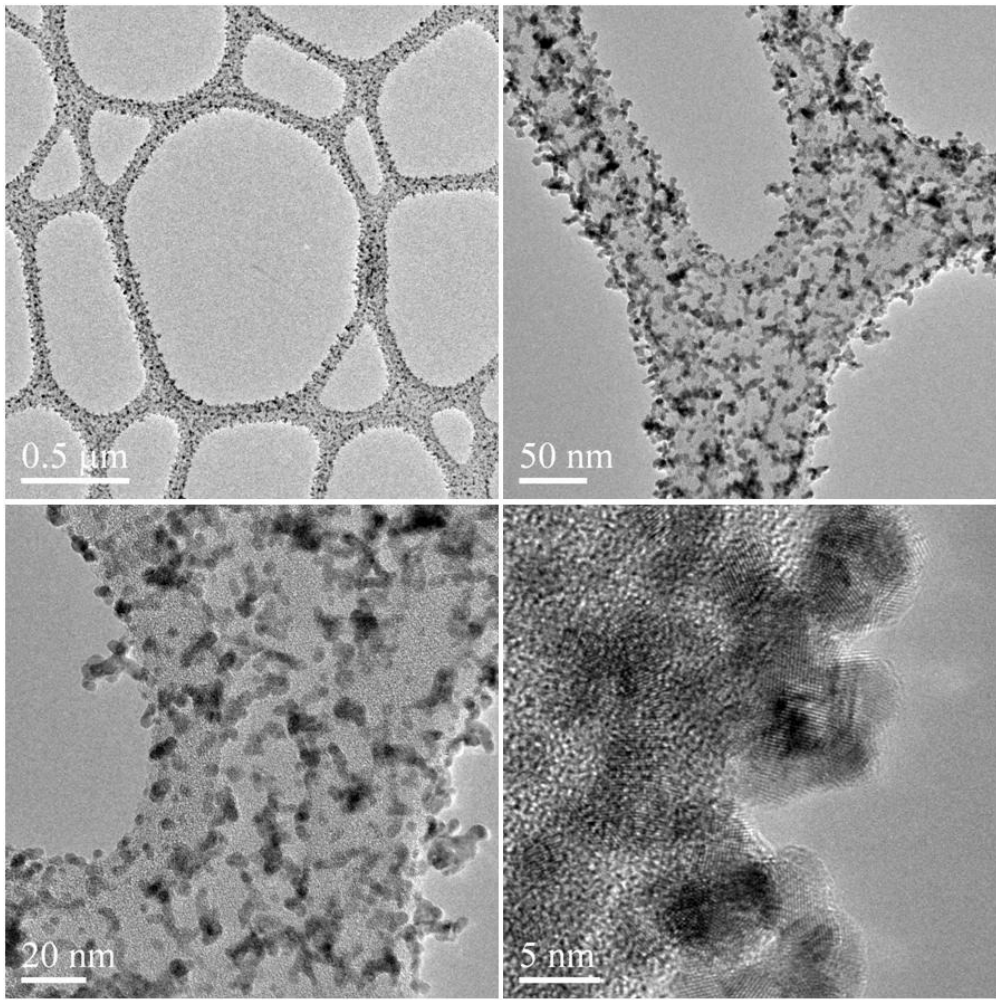


Figure 10. TEM micrographs at various magnifications of Pd particles collected on the positive electrode 1.3 cm down from ablation point

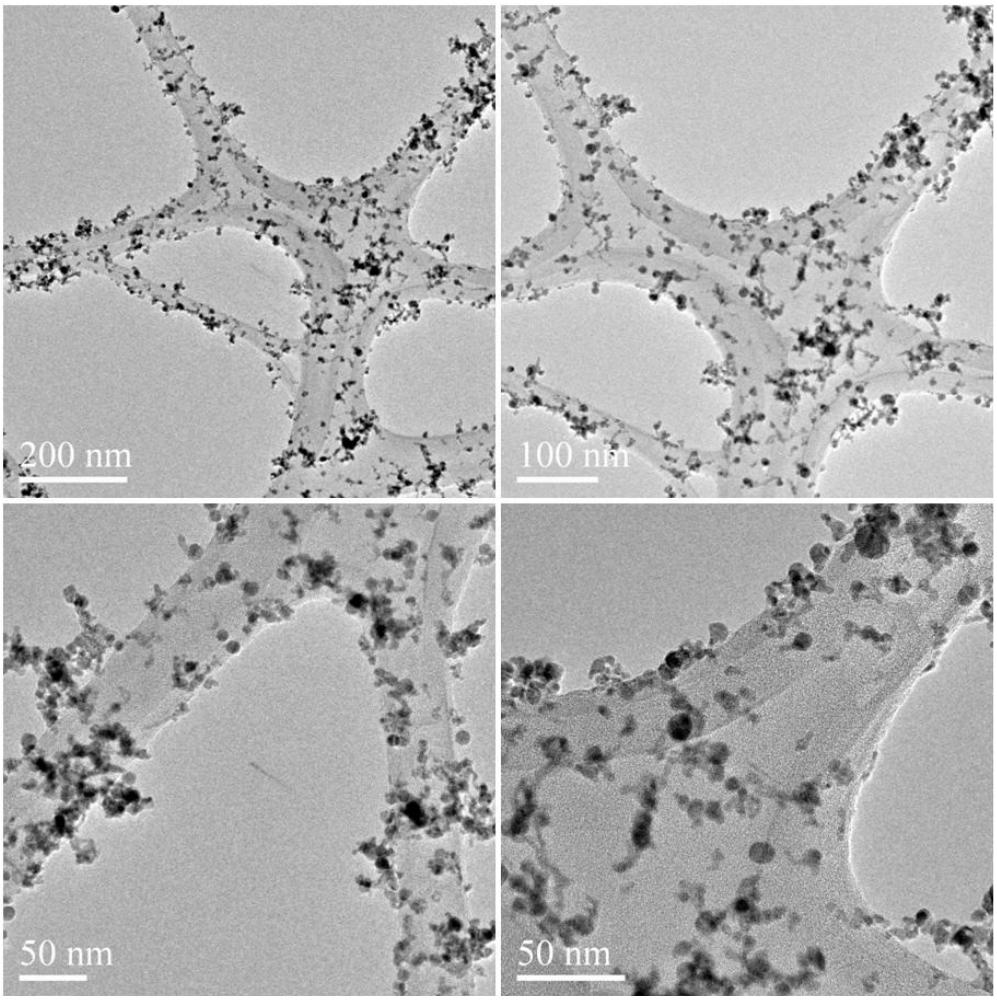


Figure 11. TEM micrographs at various magnifications of Pd particles collected on the positive electrode 6.3 cm down from ablation point

***Experiment with PEGDA***

| Feedstock material | Duration (hrs) | Average feedstock particle diameter (μm) | Approximate volume of PEGDA re-circulated (mL) |
|---|---|---|---|
| Pd | 7 | 0.5 | 30 |

Table 4. Parameters specific to Pd

The conditions of this experiment were mainly the same as the equivalent Ag and Au experiments. An approximate volume of 30 mL of PEGDA was flowed down the ground electrode and re-circulated for about 7 hrs. In order to minimize the crosslinking, the laser was not run for more than 1.25 hrs at a time. As mentioned in the previous paragraph, the Pd powder did not flow in a very constant manner. The flow in the glass tube was regularly adjusted via the by-pass valve and the feeder was regularly gently tapped in order to keep the feed rate as constant as possible. When the glass tube was tapped, very intense sparks of ablation were seen. In general, when the feed rate was reasonably high, ablation seemed more intense than for Au and Ag.

Pd nanoparticles do not have a Plasmon resonance peak in the visible range of light and hence, a colloidal suspension of Pd nanoparticles would not exhibit a specific color. Indeed, the PEGDA remained transparent throughout the experiment, which makes it difficult to estimate how much material was collected in the liquid and whether the experiment was successful. In order to check that the liquid was still flowing on the

electrode, the chamber was open after about 4.5 hrs of experiment. A 5 mL sample was taken out at this time. It was observed that the PEGDA had crosslinked on the electrode, which suggests that the liquid was indeed flowing on the electrode. Contrary to what was seen in the cases of Ag and Au, the amount of polymer that had crosslinked was less but it was spread out much further down from the ablation point. The crosslinked polymer was removed from the electrode and the experiment was resumed. Finally, about 23 mL were collected in a glass vial.

# Chapter 4: *Results*

## 4.1 Presentation and purpose of the various tests and testing methodology

Several tests and analyses were carried out on the samples produced to characterize them. Their purpose and principle are explained hereafter.

### *UV-Vis absorption*

A possible technique to characterize the concentration of metal and the nanoparticle size in PEGDA is to measure the absorbance of the liquid dispersion. To this effect, the solution is placed in a cuvette of known dimensions and illuminated by ultraviolet-visible light of known intensity. The intensity of light coming out of the cuvette is measured, and the log of the ratio of intensities gives the absorption of the solution. The concentration of the solution can then be derived from the Beer-Lambert law:

$$A = \varepsilon l c \qquad \text{Equation \# 3}$$

where A is the absorbance of the solution, ε is the extinction coefficient (in L/mol/cm), l is the length of the cuvette (usually 1 cm) and c is the concentration of the solution (in mol/L). To subtract the absorbance of the liquid medium, a baseline correction can be applied to the intensity by previously testing a blank sample (neat PEGDA in our case). The extinction coefficient depends on the material in suspension, the liquid and the wavelength of light. Some ε values are tabulated. Therefore, the concentration of

nanoparticles in suspension can be easily calculated in the case of a very narrow size-distribution and when the particle size is known.

In our case, where the sizes and size-distribution are unknown, the extinction coefficient can be calculated as a function of the particle-size-distribution function and light wavelength from the Mie Theory. Metals have the characteristic of exhibiting electron oscillations (plasmons) which interact with light and create a peak of absorbance at the plasmon resonance frequency. For most metals, the plasmon resonance is situated in the ultraviolet-visible range of the light spectrum. For a colloidal suspension of metal nanoparticles, the position and breadth of the plasmon resonance peak depends on the sizes and shapes of the particles. However, the resonance peak is usually situated around a specific wavelength for a given metal and the effect of particle size on the position shift seldom exceeds 100 nm. For small enough particles of Ag and Au (below 10 nm), the peak shift is negligible. The specific resonance peaks for small Ag and Au nanoparticles are located around 410 nm and 520 nm respectively. For Pd however, the resonance peak is located in the UV domain. This renders UV-vis analysis impossible for a Pd in PEGDA sample due to the absorbance noise caused by the PEGDA itself below 300 nm (as shown in Fig. 12). This technique was therefore only used to characterize the Ag and Au samples.

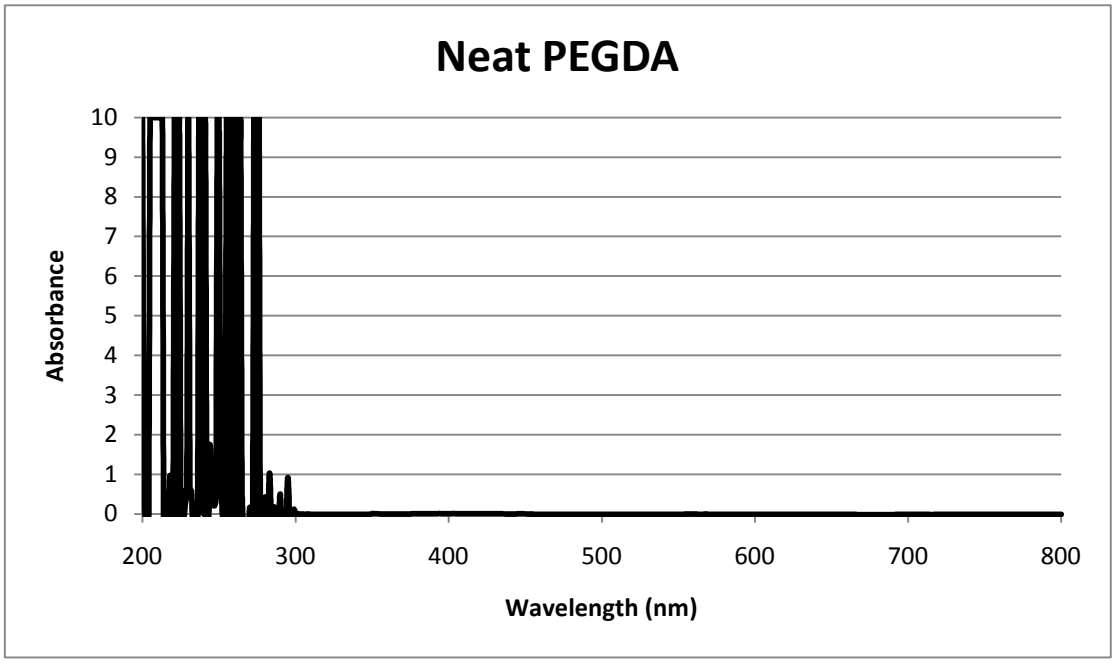


Figure 12. UV-Vis spectrum of neat PEGDA (with a baseline correction of the same sample of PEGDA)

The Mie theory gives an expression for the extinction coefficient for a spherical particle of diameter small compared to the wavelength. The data for refractive indices used in this expression were taken from the Handbook of Optical Constants of Solids (edited by E.D. Palik, 1985) and were corrected for size variations with data taken from (Kraus and Shcatz, 1983), (Bennett, 1965) and (Ashcroft and Mermin, 1976).

The UV-Vis spectra collected for Ag and Au were analyzed by comparison to the theoretical spectra, using a matlab code written by Kris Gleason (UT Austin). For this analysis, a size-distribution function (of type log-normal probability density function)

was assumed, adjusted to fit the data and compared to TEM pictures observations. An integration of Equation # 3 over wavelength then gave the total concentration of metal nanoparticles in the sample.

***X-ray fluorescence***

Another way to characterize the composition of a colloidal dispersion is to measure the X-ray photons it emits when bombarded by gamma-rays. This emission depends on the energy needed to excite an electron from an atomic orbital to another in the atom and is therefore characteristic of the element. The intensity and energy of the photons emitted make a spectrum from which the mass fraction of each element can be derived. In our case, the element is already known, only the mass fraction is unknown. It is therefore possible to analyze only one energy specific to the given element. The energy chosen for our analysis is that of the $K_\alpha$ transition (from the K orbital to the L orbital). The values of interest are 22.16 keV for Ag, 68.8 keV for Au (37) and 21.18 keV for Pd (38). The radioactive source used was $^{57}$Co.

By using a blank sample and a calibration sample, the investigated concentration can be inferred by interpolation according to the following relationship:

$$C = C_{cal} \times \frac{n - n_b}{n_{cal} - n_b} \qquad \text{Equation \# 4}$$

Where $C$ and $C_{cal}$ are the concentrations of the investigated sample and the calibration sample respectively and $n$, $n_b$ and $n_{cal}$ are the the number of counts at the specific energy for the investigated sample, the blank sample and the calibration sample respectively. The

blank sample is usually the neat liquid medium (in our case neat PEGDA). The calibration sample needs to contain the given element in a known concentration. Here, a dispersion of microparticles of the given metal in PEGDA was used as the calibration sample.

***Membrane formation***

In order to test its permeation, a membrane film must be made from the liquid sample. 5 g of PEGDA sample is sufficient to make enough films for all the required tests. The sample is first sonicated and heated for 1 hr in order to break up the possible agglomerates and flocculates. A photo-initiator (1-hydroxycyclohexylphenylketone) is then added (6 mg for every g of PEGDA solution) and the mixture is stirred for 1 hr. A few drops are placed between two glass plates separated by spacers (0.254 mm) and exposed to UV radiation in a spectrolinker (312 nm) for 90 s. The setup must be leveled in order to have a homogeneous film thickness. Bubbles should be avoided as they will influence the permeation test. The resulting membrane should be rubbery.

***Permeation/selectivity with the various gases***

The permeation measurement depends on the thickness of the membrane tested and the pressure difference on either side of the membrane, as described by equation # 5 (39). Film thickness and pressure difference are therefore measured in order to normalize

the various permeation measurements for different membranes. The steady-state permeability *P* is given by:

$$P = \frac{N.l}{p_2 - p_1} \qquad \text{Equation \# 5}$$

where *N* is the one-dimensional gas flux through the membrane, $p_2$ and $p_1$ are the upstream (high) and downstream (low) pressures, respectively. The common unit used for permeability is the Barrer which is defined as:

$$Barrer \equiv 10^{10}.\frac{cm^3(STP).cm}{cm^2.s.cmHg} \qquad \text{Equation \# 6}$$

where STP stands for Standard Temperature and Pressure of the gas tested.

Film thickness is measured with a digital micrometer. However, for rubbery polymers such as PEGDA, the measuring tip often penetrates into the membrane resulting in an underestimated value for film thickness. Upstream and downstream pressures are measured using commercial pressure gauges.

There are several methods of measuring the selectivity of a membrane. The flux through the membrane can be a mixture of the two gases investigated. The permeability of each gas can also be measured independently with pure gas fluxes. Those independent measurements can be carried out at constant pressure with variable volume or at constant volume with variable pressure. In our case, the permeation of each gas was measured independently at constant volume and variable pressure. The permeation cell consists in a flange containing the membrane (reduced to the cell size) supported by a metal mesh. An O-ring prevents the gas from leaking between upstream and downstream compartments without passing through the membrane. The cell is bathed in liquid kept at a constant

temperature of 35°C to prevent potential temperature change from influencing the permeability. The two compartments of the cell are connected to a vacuum pump by valves (as shown in Fig. 13). Both compartments are first evacuated. When the vacuum valves are closed, a pressure rise, which stems from leakage, can be observed in the downstream compartment. This rate is recorded and later subtracted to the measured rate of pressure rise (see Eq. # 7). The gas is then fed in the upstream compartment while the pressure rise is measured in the downstream compartment.

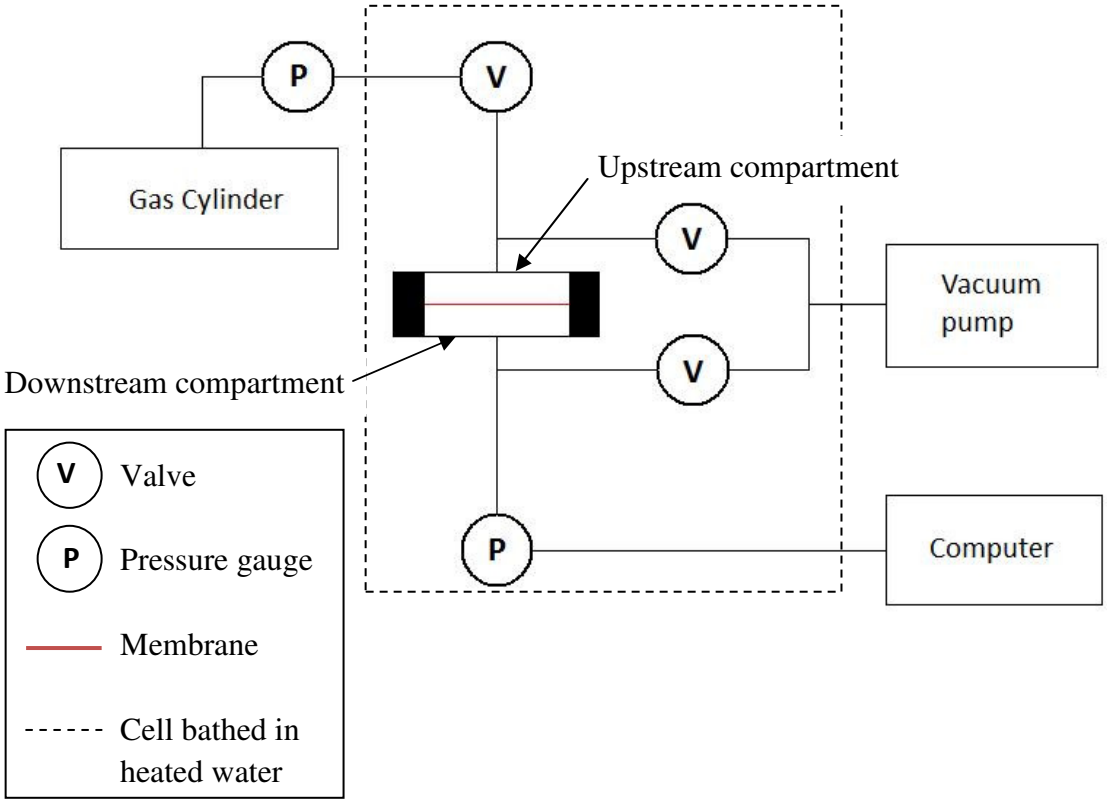


Figure 13. Schematic of permeability measurements setup. Redrawn from (39)

The permeability can be determined from:

$$P = \frac{V_d . l}{p_2 . A . R . T}\left[\left(\frac{dp_1}{dt}\right)_{ss} - \left(\frac{dp_1}{dt}\right)_{vac}\right] \qquad \text{Equation \# 7 (39)}$$

where $V_d$ is the volume of the downstream compartment, $A$ is the film area available for gas transport, $R$ is the gas constant, $T$ is the absolute temperature and $\left(\frac{dp_1}{dt}\right)_{ss}$ and $\left(\frac{dp_1}{dt}\right)_{vac}$ are the steady-state pressure rises in the downstream compartment at fixed upstream pressure and under vacuum, respectively (39).

The aim of measuring sorption (or solubility) is to understand the effect of the presence of carriers in facilitated transport membrane. Permeability is the product of solubility and diffusivity. Therefore, a change in permeability can be attributed to either a change in solubility, diffusivity or both. Since diffusivity is less practical to measure, it is often inferred from the solubility and permeability measurements. There are several methods for measuring solubility. The one used here is the dual-volume pressure decay method (39). The setup consists of a sample cell containing the membrane and connected to a vacuum pump and a charge cell connected to a gas cylinder. The two cells are connected to each other. The sample cell is first evacuated and the charge cell is filled with gas to a known pressure. Some gas is then flowed from the charge cell to the sample cell. The number of moles passed from one cell to the other can be inferred from the pressure drop in the charge cell. The pressure in the gas phase of the sample cell will decrease as the gas is sorbed into the polymeric membrane. Pressure drop can be recorded over time. When the pressure in the sample cell reaches a stable value, equilibrium is attained. The number of moles of gas remaining in the sample cell can be calculated from

the equilibrium pressure. Therefore, the number of moles sorbed by the polymer is calculated as the difference between the initial and equilibrium numbers of moles in the gas phase of the sample cell. The procedure is then iterated by adding more gas to the sample cell in order to get solubility as a function of pressure.

For the results presented below, the permeability and solubility measurements for Au and Ag were carried out by Ralm Ricarte and the measurements for Pd were carried out by Zachary Smith, at the Pickle Research Center (UT Austin).

## 4.2 Silver

### *TEM observations*

Pictures of the dry grids placed at the two extreme positions (1.5 cm and 16.5 cm) were taken at various magnifications with a JEOL 2010F TEM. On the grid placed 1.5 cm down from the ablation point, pictures show a high density of particles, a small average particle size (estimated at 5 nm), a narrow size-distribution range (estimated between 2 nm and 10 nm) and particles that are all individual and not agglomerated (as shown in Fig. 14).

On the grid placed 9 cm down from the ablation point, pictures show a lower density of particles, a larger average particle size (estimated at 10 nm) and a few small agglomerates or sintered particles, although most particles remain individual (as shown in Fig. 15).

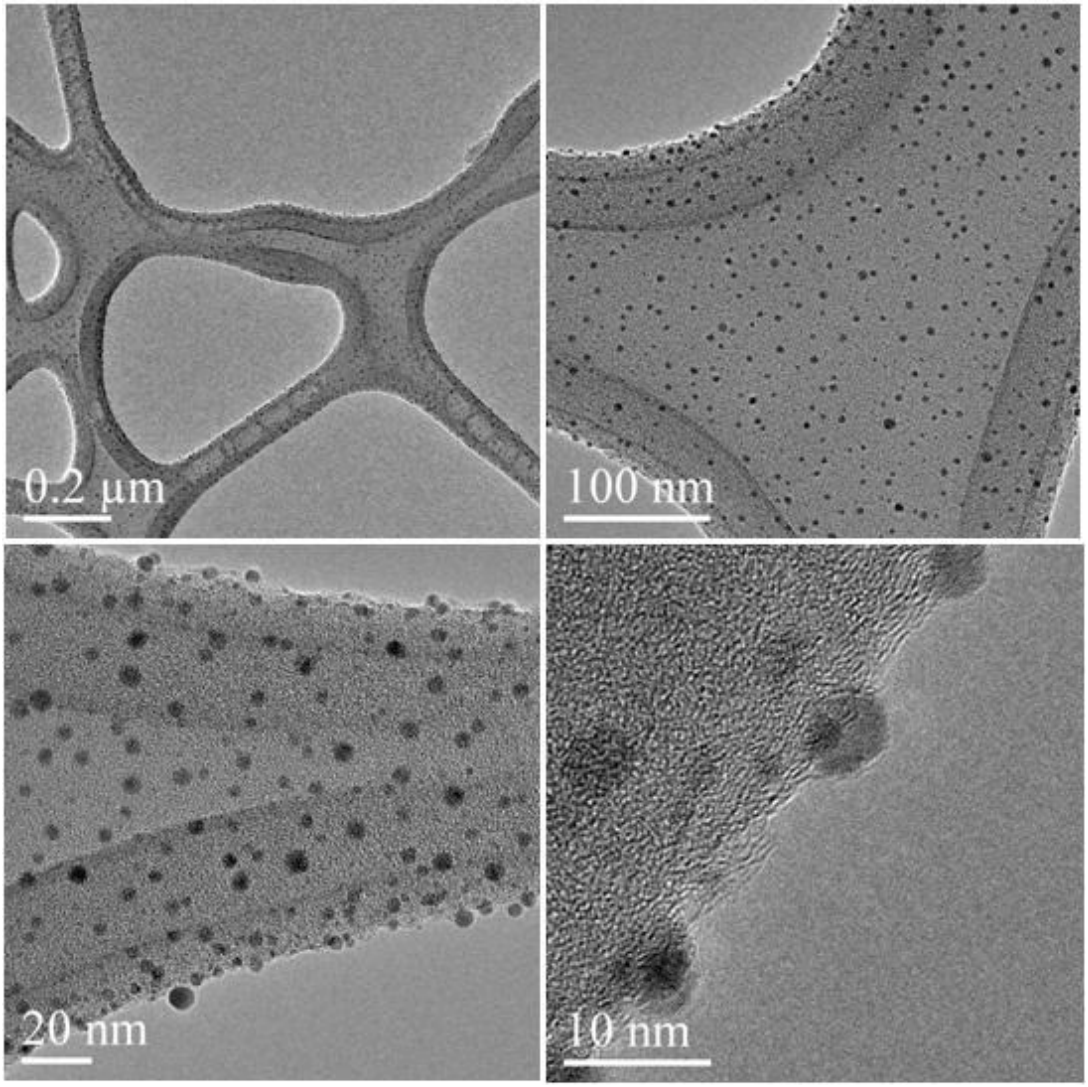


Figure 14. TEM micrographs of Ag nanoparticles collected 1.5 cm down from ablation point

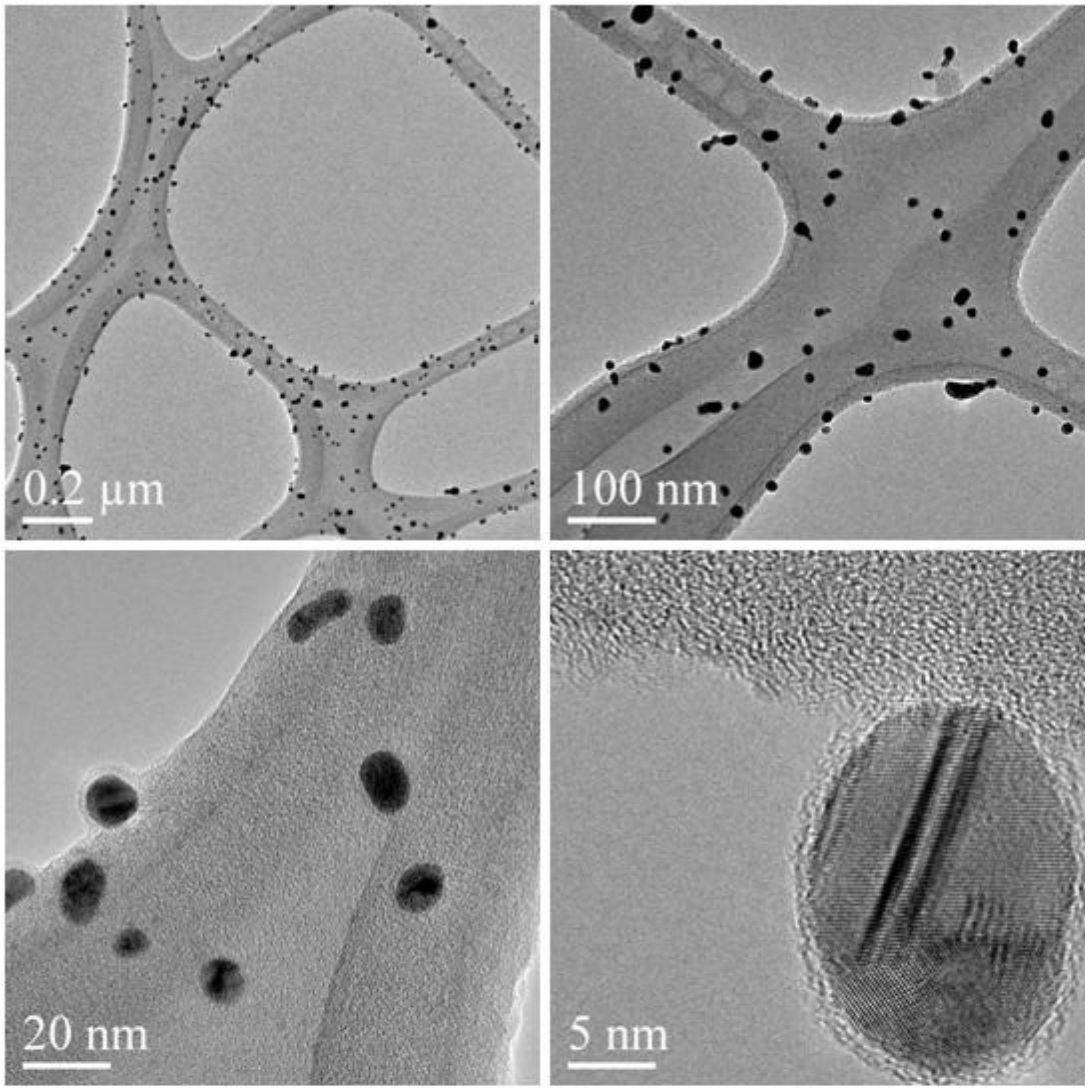


Figure 15. TEM micrographs at various magnifications of Ag nanoparticles collected 9 cm down from ablation point

This clear size difference between the two positions confirms that electrostatic collection is size selective depending on the collection distance to the ablation point. It also suggests that the size range of particles in the PEGDA should include at least this

breadth of sizes (which is a rather narrow size-distribution altogether). Finally, this shows that the particles hardly agglomerate throughout the production and collection process. It is possible however, that they agglomerate once in suspension in the liquid.

***TEM images of PEGDA sample***

Images of sample A (1 drop of PEGDA-Ag + 2 mL of ethanol, shaken not stirred) show some very large agglomerates made up of larger particles than seen in the dry grids that seem sintered together (as shown in Fig. 16). This confirms that particles agglomerate once in the liquid, as it re-circulates and collects more particles. However, it could also be that most particles are not actually sintered together but connected by liquid remaining on the grid and around the particles. The fact that many particles exhibit a non-circular shape and the large black areas seen on the grid (top left picture of Fig. 16), support the latter hypothesis. EDS analysis was carried out on those black areas and did not show any silver whereas EDS carried out on the agglomerate showed that they consisted of silver particles. It is therefore very likely that some liquid (or maybe crosslinked PEGDA) remains on the grids and it seems that particle agglomerates are mostly found attached to those areas.

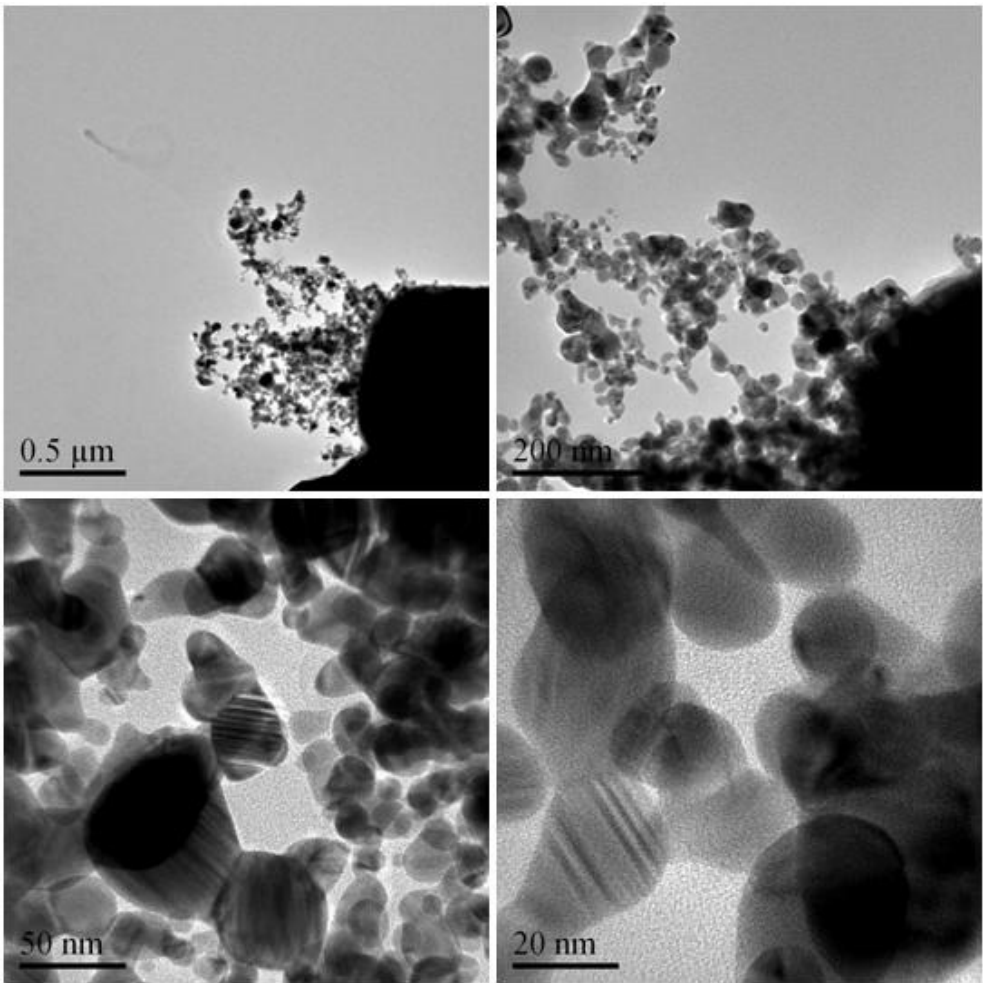


Figure 16. TEM micrographs at various magnifications of sample A (1 drop of PEGDA-Ag + 2 mL of ethanol)

It should be noted that particles were not easily found on the grid. Very few of these agglomerates were observed. It is possible that the particles covered in some liquid become very hard to observe in the TEM. It is then safe to assume that there was possibly a fair amount of individual particles spread throughout the grid.

As mentioned earlier, the 5 mL sample collected was completely balck. However, after being left to sit for about 2 weeks, the sample had become completely transparent with a few small balls of black material deposited at the bottom. This sample was then sonicated. During the first 30 min of sonication, the black material spread out at the bottom and covered the entire section of the vial. After several hours of sonication, the sample color had slowly become yellowish-grey and a fair amount of black material had remained at the bottom. Further sonication did not seem to change this situation. However, shaking the sample manually returned it to its original black color. This suggests that the major part of the silver contained in the sample consists of large agglomerates (black material remaining at the bottom) while there are still enough small nanoparticles to yield a yellowish grey color.

***UV-Vis Spectra***

The UV-Vis spectrum taken from the black Ag sample (see Fig. 17) shows a peak at 408 nm characteristic of the presence of Ag nanoparticles. This peak is very broad which suggests that the size-distribution is also broad, and absorbance remains high through 800 nm which suggests the presence of agglomerates in the solution. The high value of absorbance (around 1.2) correlates to the dark color of the sample and is certainly due to the large agglomerates.

The data was fitted with the Mie calculation model. The model did not adjust well to this data, probably due to the large number of agglomerates which the model does not account for (one of the assumptions being that the particles are much smaller than the wavelength). The best fit was thus chosen for the broadest possible peak and for matching peak positions, as shown on Fig. 17. This fit corresponds to a log-normal probability distribution with a mean particle size of 2 nm. The fitting was not very sensitive to standard-deviation variations and is most likely representative of only the small particle distribution present in the yellowish-grey part of the sample.

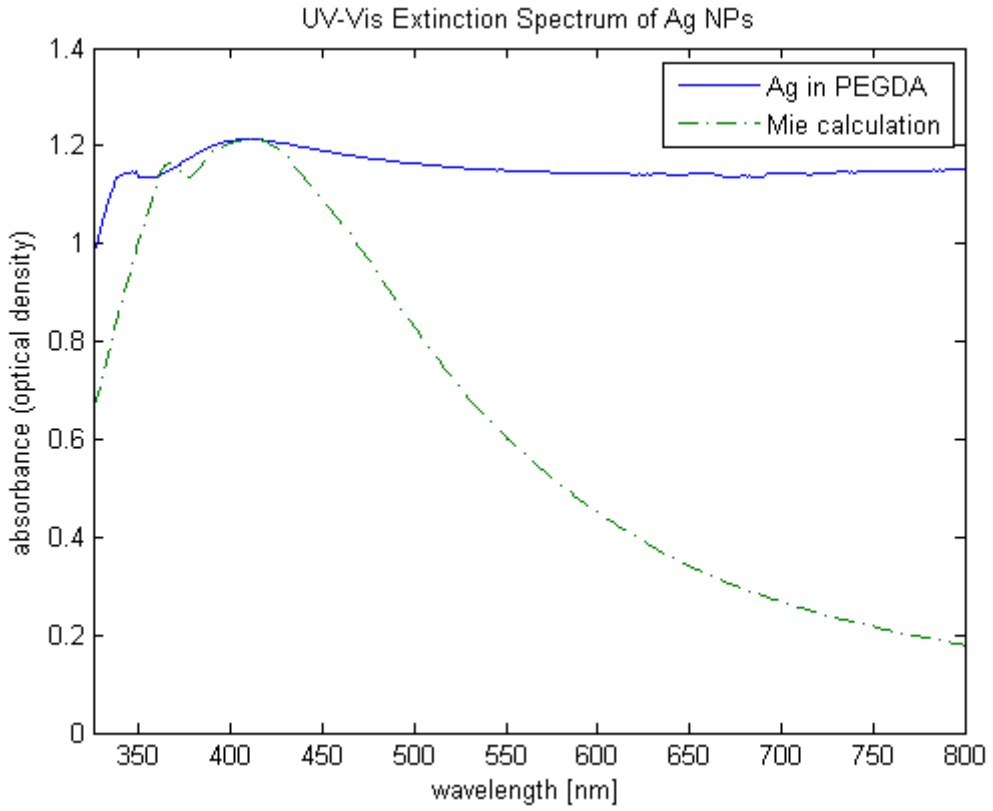


Figure 17. UV-Vis spectrum of Ag in PEGDA sample, fitted with Mie model

Using this size-distribution and the Mie theory for the calculation of the extinction coefficient, the mass fraction of Ag in the sample was calculated to be of the order of 14 ppm. It is probably higher than that in reality given the difference in the UV-Vis spectra, but the order of magnitude gives an under-estimate of the true mass fraction.

***X-ray fluorescence data***

The calibration sample was prepared by mixing (shaken manually) 0.0205g of Ag microparticles (same Dupont® powder as used for experiments) in 5 mL of PEGDA. The density of PEGDA being 1.1 g/cm$^3$, the mass fraction of the calibration sample was $C_{cal}$ = 0.37 wt% (3700 ppm) of Ag in PEGDA. The number of counts collected were $n_b$ = 52503, $n_{cal}$ = 80975, $n$ = 55774, yielding a mass fraction for the investigated sample of $C$ = 0.04 wt% (400 ppm).

Since the technique has a detection limit of 200 ppm and given the large error that exists in determining the number of counts, it can be said that the concentration of the sample is barely detectable. This tends to show that the concentration is indeed higher than the 14 ppm estimated by UV-Vis analysis. It also shows the difficulty of estimating the amount of Ag in PEGDA.

***Permeation/selectivity data***

Four different films cast from the same sample were used for the permeability measurements with the four different gases (propylene, propane, ethylene and ethane). For each film, the thickness was averaged over 12 measurements and the area available for permeation was calculated using a die diameter averaged over 5 measurements. The downstream pressure was measured at 4 different upstream pressures (172, 345, 517 and 689 kPa). The pressure rise is derived from the measurements of downstream pressure over time. The results, gathered in Appendix A, are inputted into Equation #7 to calculate permeability of this membrane to the gas tested. Temperature is kept constant at 308.15 K for all tests. Selectivity and permeability are shown in Table 5. These results are compared to other samples and discussed in Chapter 5.

| Upstream pressure (kPa) | Ethylene/Ethane selectivity | Ethylene permeability (barrer) | Propylene/Propane selectivity | Propylene permeability (barrer) |
|---|---|---|---|---|
| 172 | 1.96 | 31.3 | 2.52 | 53.6 |
| 345 | 1.96 | 32.0 | 2.49 | 56.0 |
| 517 | 1.96 | 33.0 | 2.53 | 60.8 |
| 689 | 1.96 | 33.7 | 2.62 | 67.6 |

Table 5. Selectivity and permeability measured for Ag in PEGDA membranes at different pressures. Data from Ralm Ricarte

## 4.3 Gold

***TEM observations***

Pictures of the grids placed at the two extreme positions (1.5 cm and 16.5 cm) were taken at various magnifications with a JEOL 2010F TEM. Observations are very similar to those for the equivalent Ag pictures.

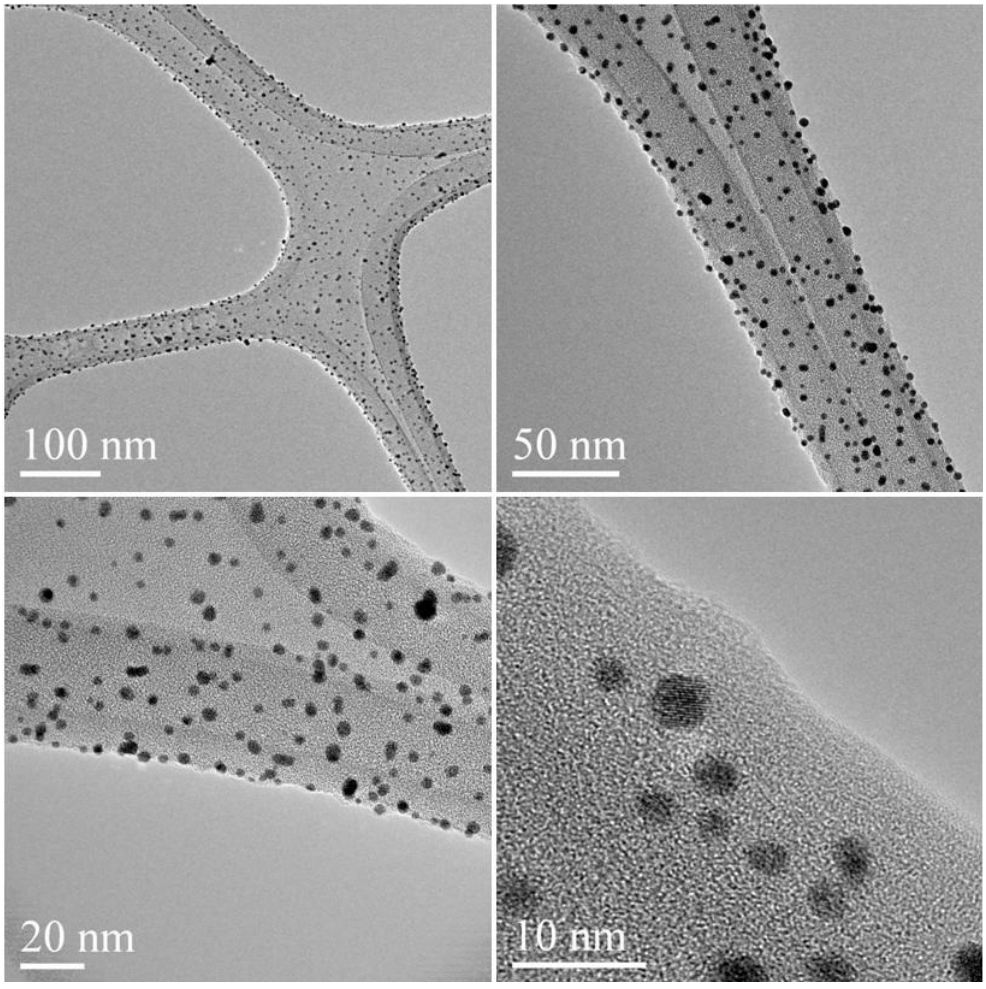


Figure 18. TEM micrographs at various magnifications of Au nanoparticles collected 1.5 cm down from ablation point

On the grid placed 1.5 cm down, shown in Fig. 18 there is a high density of particles on the grid, nanoparticles are mostly individual and small with a rather narrow size-distribution. The average particle size is estimated at 5 nm. On the grid placed 16.5 cm down, shown in Fig. 19, there are fewer but larger particles and small agglomerates. Those pictures again show a size-selection of particles very clearly.

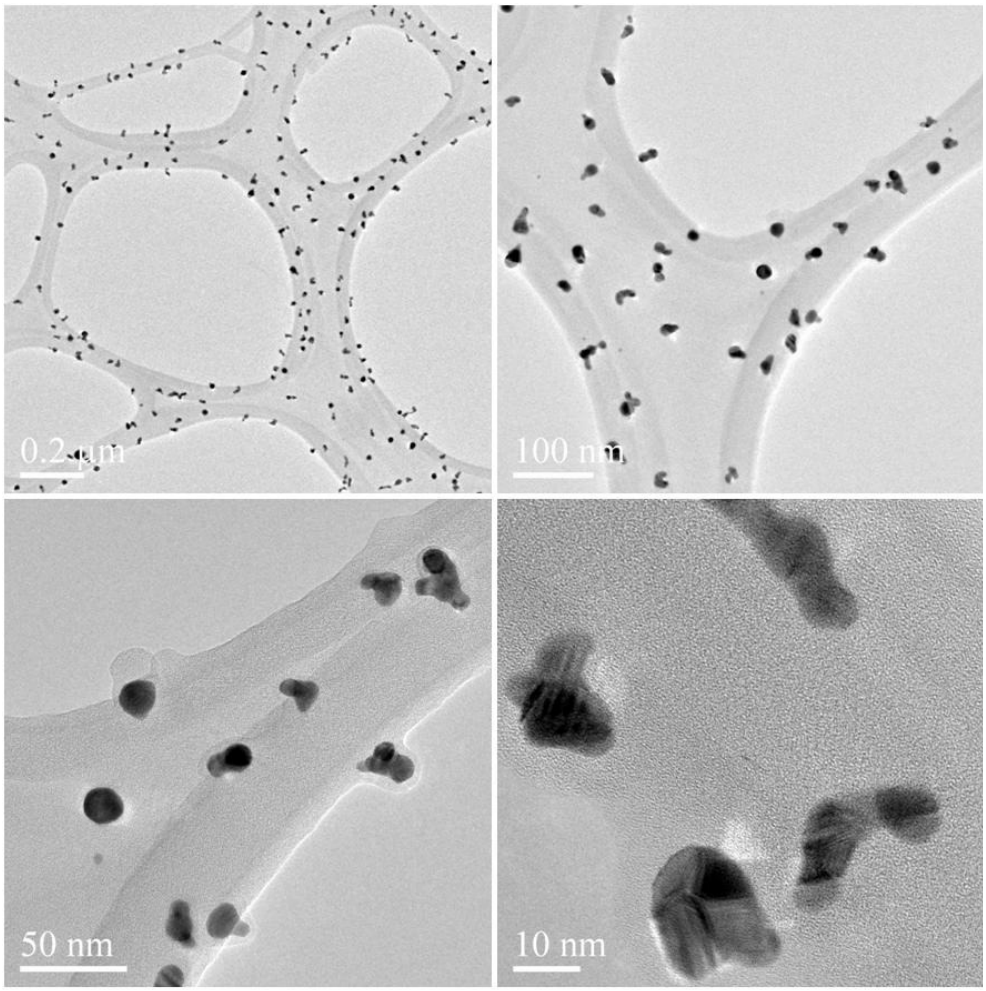


Figure 19. TEM mircographs at various magnifications of Au nanoparticles collected 16.5 cm down from ablation point

***UV-Vis Spectra***

The UV-Vis spectrum taken from the Au sample (see Fig. 20) shows a peak at 541 nm. The peak is narrower than observed in the Ag sample, and the absorbance decreases steadily up to 800 nm which suggests a narrower size-distribution and probably fewer agglomerates in the sample. This correlates with the observations of the sample (less material deposited at the bottom). The overall absorbance of the sample (around 0.2) is much lower than that of the Ag sample (around 1.2). The data was fitted using the Mie model. The best fit, shown in Fig. 20, was found to match a mean particle size of m = 4.5 nm, which is in agreement with the TEM observations.

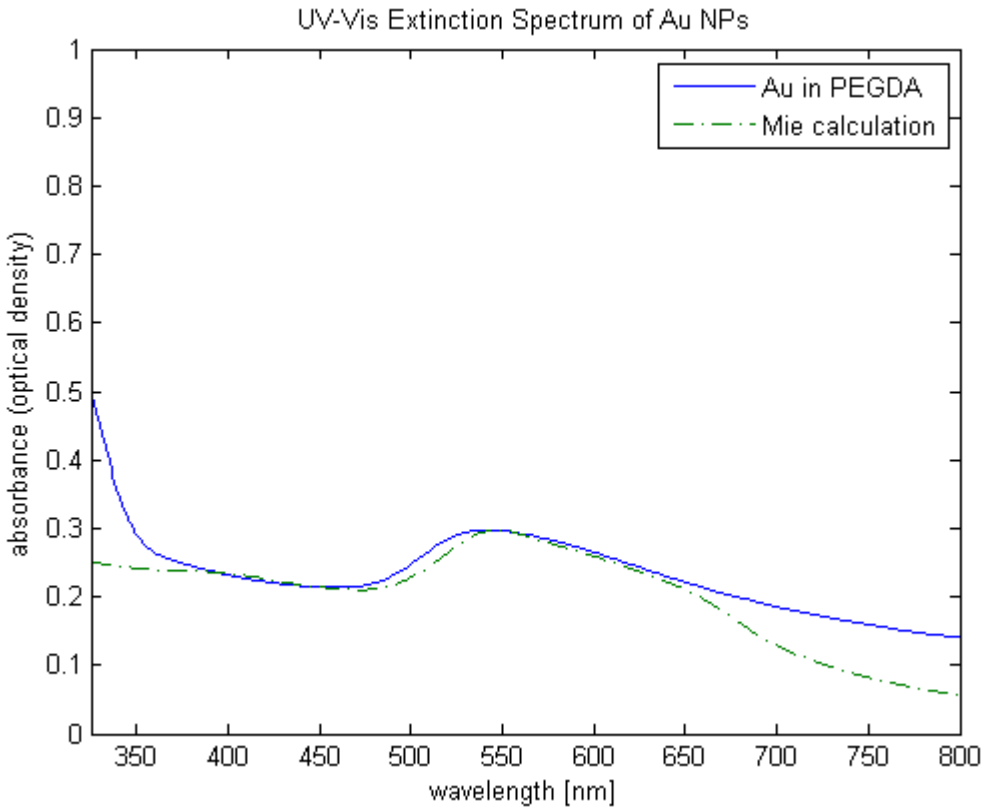


Figure 20. UV-Vis spectrum of Au in PEGDA sample, fitted with Mie model

Kris Gleason's Matlab program was modified in order to fit the model by adjusting m and s, respectively the mean and standard deviation of the log-normal distribution. It assumes a log-normal probability density function with parameters μ and σ (respectively the mean and standard deviation of the associated normal distribution). These parameters were computed using Equations #8 and 9 (40) (inserted in the program in place of the original μ and σ expressions). The log-normal probability density function expression is given in Equation #10. Again, the fitting was not very sensitive to variations in s.

$$\mu = \ln\left(\frac{m^2}{\sqrt{s^2 + m^2}}\right) \qquad \text{Equation \#8}$$

$$\sigma = \sqrt{\ln\left(\frac{s^2}{m^2}\right) + 1} \qquad \text{Equation \#9}$$

$$lognpdf(x, \mu, \sigma) = \frac{1}{x\sigma\sqrt{2\pi}} e^{\frac{-(\ln(x)-\mu)^2}{2\sigma^2}} \qquad \text{Equation \#10}$$

Using this size-distribution and the Mie theory for the calculation of the extinction coefficient, the mass fraction of Au in the sample was calculated to be of the order of 7 ppm. Given this result and the observation that the Au sample seems to contain less metal than the Ag sample (which was close to the detection limit for XRF), XRF analysis was not carried out on the Au sample.

***Permeation/Selectivity graphs and data***

Measurements were taken similarly to the Ag sample. Details are gathered in Appendix B. Permeability and selectivity for the Au in PEGDA sample are compared to other samples and discussed in Chapter 5.

| Upstream pressure (kPa) | Ethylene/Ethane selectivity | Ethylene permeability (barrer) | Propylene/Propane selectivity | Propylene permeability (barrer) |
|---|---|---|---|---|
| 172 | 2.04 | 31.4 | 3.40 | 49.7 |
| 345 | 2.06 | 32.1 | 3.03 | 52.7 |
| 517 | 2.01 | 33.0 | 3.08 | 61.9 |
| 689 | 1.96 | 33.7 | 3.14 | 72.0 |

Table 6. Selectivity and permeability measured for Au in PEGDA membranes at different pressures. Data from Ralm Ricarte

## 4.4 Palladium

***TEM observations***

Pictures of the dry grids placed at the two different positions (1.5 cm and 9 cm) were taken at various magnifications with a JEOL 2010F TEM. The grid placed further

down along the electrode (16.5 cm) did not show any particles suggesting that there were few large particles ( > 50 nm) or agglomerates produced and that the flows were laminar. As for the equivalent experiments with Ag and Au, the grid placed at 1.5 cm shows a high density of very small particles (average size below 5 nm) and a very narrow size-distribution, as can be seen on Fig. 21. It should be noted that EDS analysis was not carried out on these grids. It is, however, assumed that the particles observed are Pd.

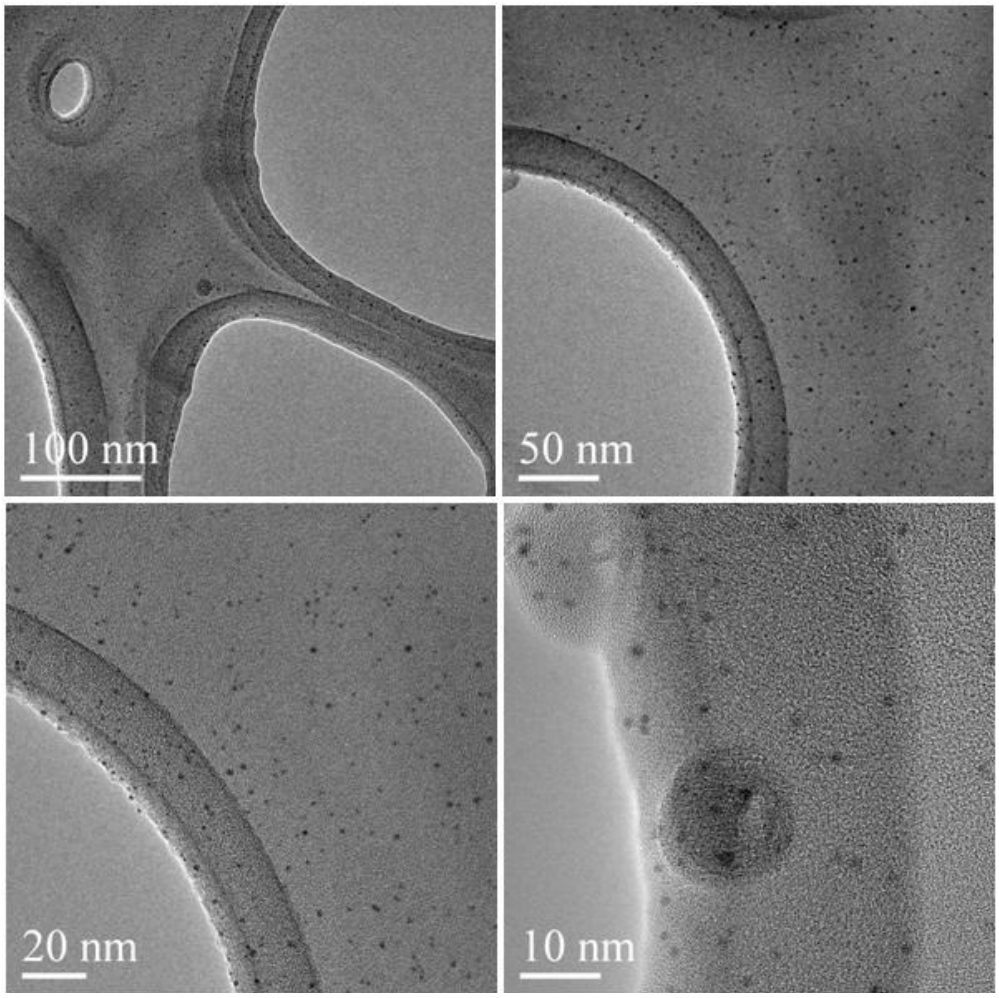


Figure 21. TEM micrographs at various magnifications of Pd nanoparticles collected 1.5 cm down from the ablation point

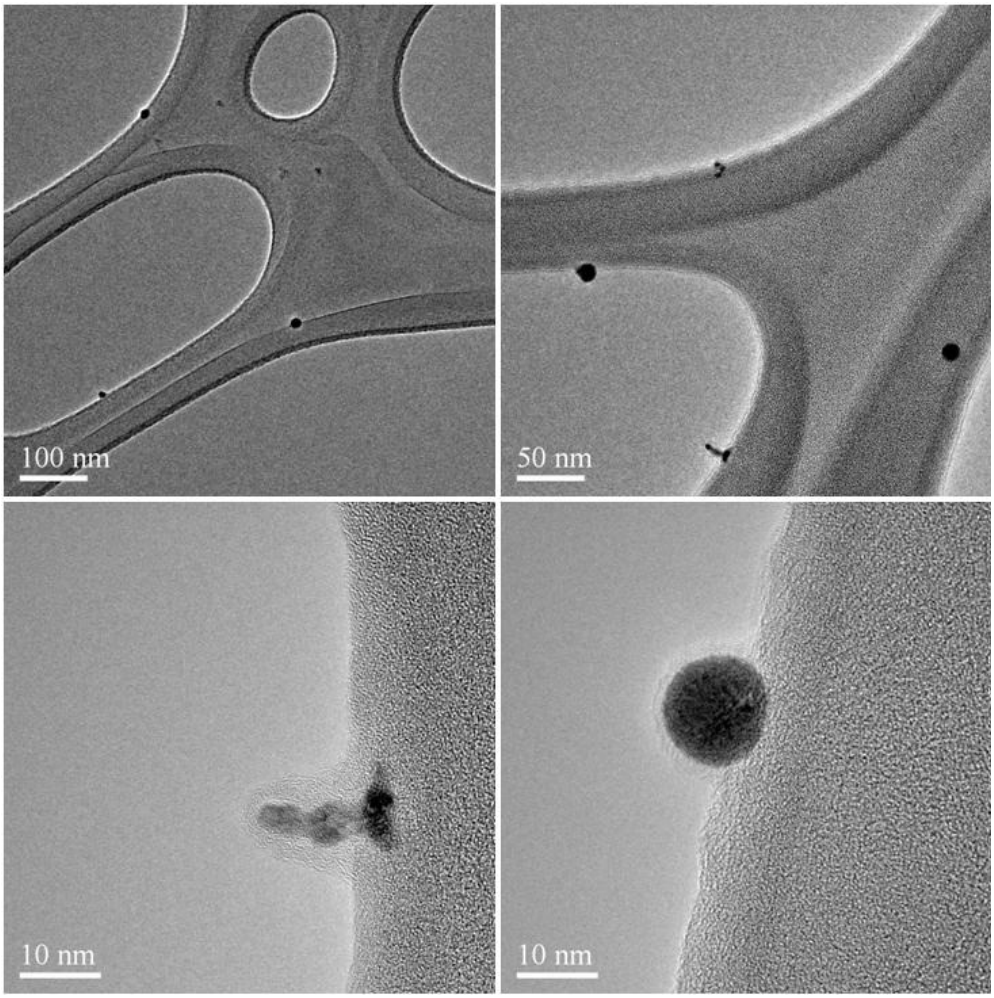


Figure 22. TEM micrographs at various magnifications of Pd nanoparticles collected 9 cm down from the ablation point

The grid placed at 9 cm down from the ablation point (see Fig. 22) showed larger particles (average size estimated at 15 nm) and agglomerates of small particles, again demonstrating the size-selection of the electrostatic collection technique. The density of

particles on the grid was also much lower which seems to confirm the previous observation that this process produces relatively few large particles and agglomerates.

***Mass fraction analysis***

Pd in PEGDA is not characterizable by UV-Vis spectroscopy, as explained previously. It is very unlikely that the Pd sample would contain much more material than the Ag and Au samples. Given the estimated mass-fractions of those samples, it can be assumed that the Pd sample would also lie below the detection limit for XRF analysis. The mass-fraction of Pd in PEGDA is therefore unknown but it is reasonable to assume that it would be of the same order of magnitude as the Au sample.

***Permeation/Selectivity graphs and data***

Measurements were not taken at the time of the writing of this thesis. They will be performed by Zachary Smith in a similar way to the measurements on the Ag and Au samples, and available in the UT Digital Repository (41).

# Chapter 5: *Discussion*

## Discussion of facilitated transport membranes

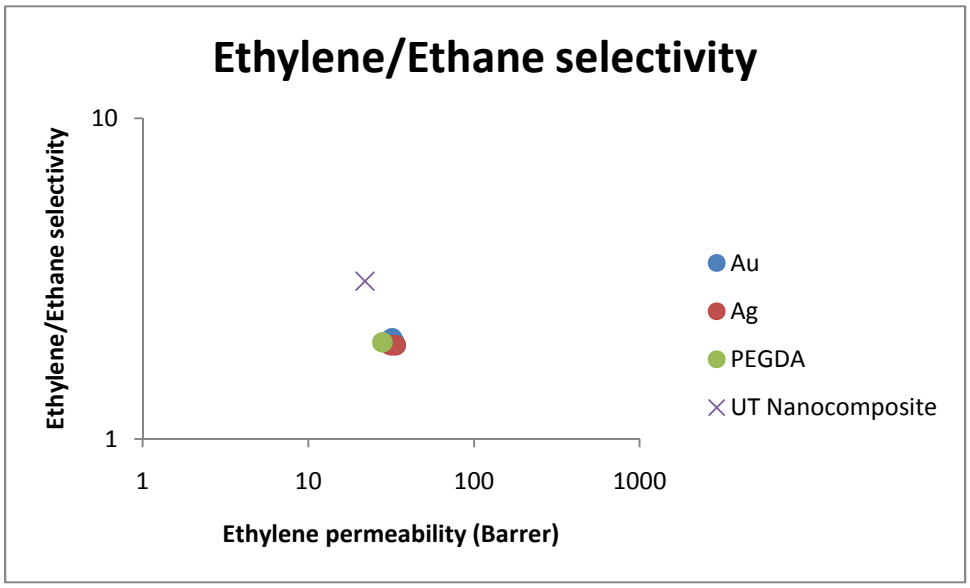


Figure 23. Comparative plot of ethylene/ethane selectivity for various membranes

Membranes of Ag and Au embedded in PEGDA were tested to investigate their possible use as facilitated transport membrane. The results are gathered on Figs. 23 and 24 and compared to neat PEGDA, to the conventional polymer membranes (the upper bound represents the best results yet achieved by conventional polymer membranes) and to the original data point obtained with the UT Nanocomposite (Ag in PEGDA). It seems that the membranes produced via LAMA with electrostatic collection behave similarly to neat PEGDA. Selectivity was not enhanced by the presence of metal nanoparticles.

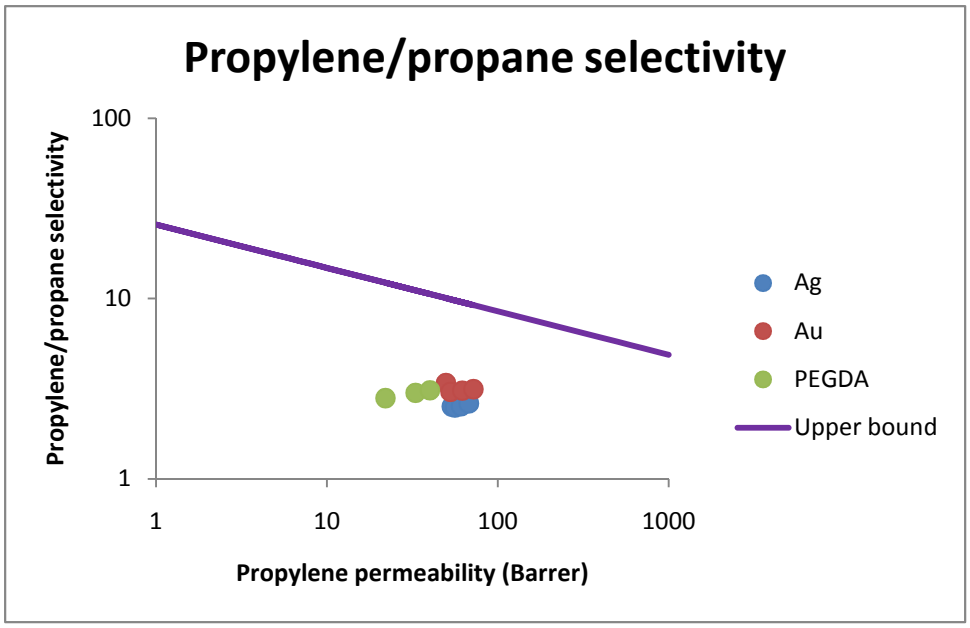


Figure 24. Comparative plots of propylene/propane selectivity for various membranes

Characterization of the samples showed that the amount of metal contained in the PEGDA was very low. It is quite possible that selectivity enhancement is dependent on the particle concentration and that the mass fractions needed to observe a change in behavior are much higher than the ones achieved with our method. Given the long production time (~7 hrs) for these samples and the observation that particles start to agglomerate in the liquid after a few hours, the LAMA process used with electrostatic collection does not appear to be the best technique for production of facilitated-transport membrane containing nanoparticles. Permeability and selectivity results for the Pd sample are still awaited. Conclusions are not expected to change but judgment is reserved until the results are obtained.

## Discussion of other results

Other observations made during this project could be of greater interest. The TEM pictures collected on the ground electrode for the various metals mostly show individual nanoparticles. The TEM pictures collected on the positive electrode show a large amount of material, mostly agglomerated particles (as seen in Figs. 10-11). It can be inferred that recombination occurs fast enough for a high percentage of the particles to be affected by it before they escape the electron cloud. It then seems obvious that the electrostatic collection technique can never yield very high production rates. This technique should therefore be used if focus is on the quality of particles rather than quantity.

Indeed, observations of TEM pictures also showed striking size-selection (as summed up in Fig. 25). As mentioned in Chapter 1, nanoparticle properties (optical (42), magnetic, catalytic, thermodynamic, electronic…) have been shown to be highly size-dependent. Tunability of particle size is therefore a major challenge for nanotechnologies. The production technique presented in this thesis could therefore find many applications in various fields. Moreover, experimental studies of size-dependence of many properties are needed to correlate with models and theoretical studies. Such studies can only be carried out on particles with a very narrow size-distribution. Individual, size-controlled nanoparticles produced by LAMA and collected electrostatically could be used for a better understanding of size-dependent properties in the nanoscale regime.

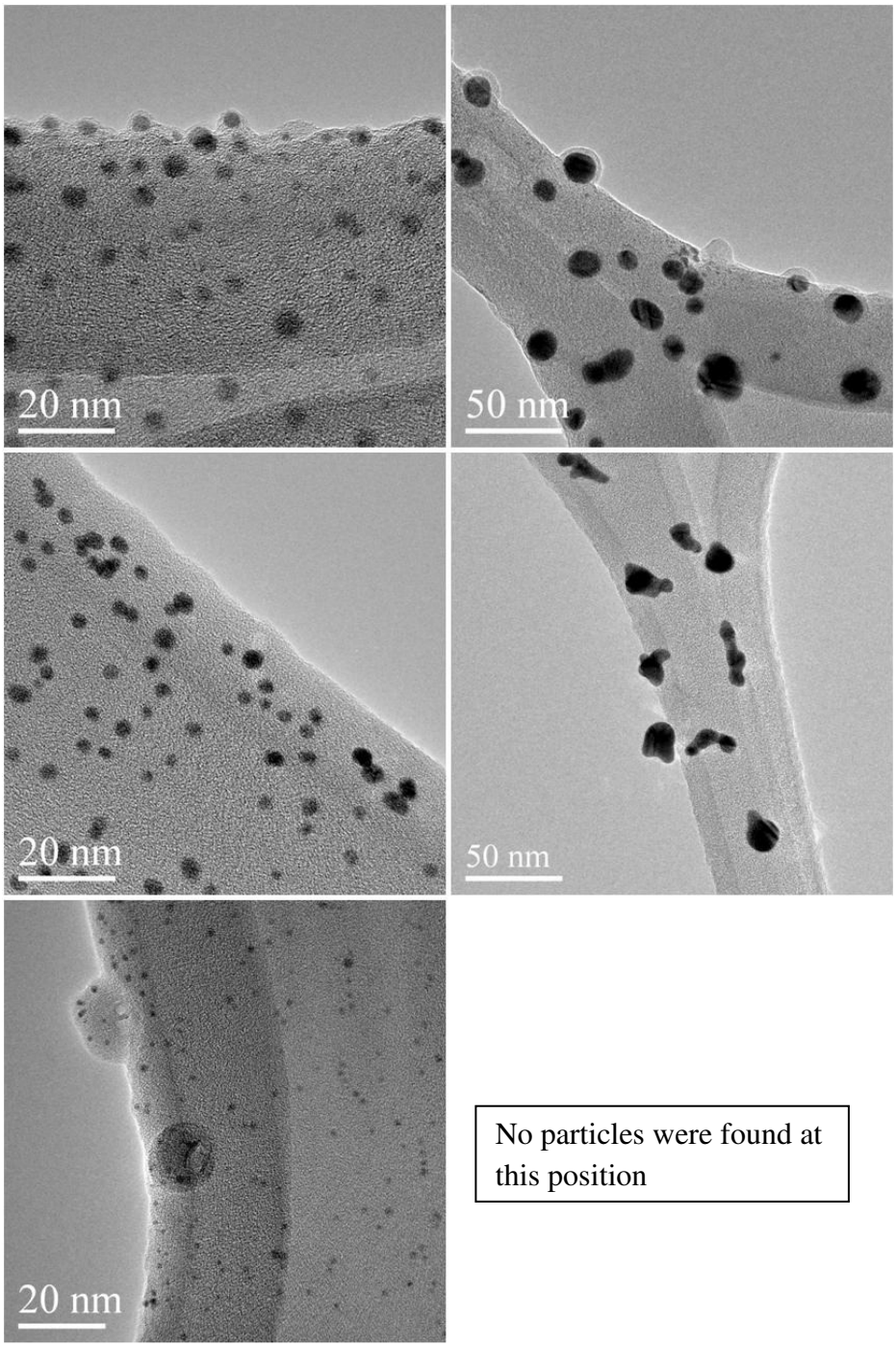


Figure 25. Comparison of TEM micrographs of Ag (top), Au (middle) and Pd (bottom) collected about 1.5 cm (left) and 16.5 cm (right) down from ablation point

# Chapter 6: *Conclusion and future work*

The objective of this work was to study the LAMA process with electrostatic collection, focusing on a particular application for the nanoparticles produced (facilitated-transport membranes for olefin/paraffin separation). The conclusion can be drawn that this process is not applicable to this purpose. However, other possible applications for this process appeared during the project. The LAMA process coupled with electrostatic collection produces individual, bare nanoparticles and shows a very efficient size-selectivity. The main disadvantage of this technique is the low collection efficiency, as few particles remain charged long enough to participate in size-selection. Nanoparticle size control is a major asset for many applications, as particle properties become appreciably size-dependent in the nanoscale regime. Few production techniques so far show the ability to control the size of nanoparticles with as much precision. A wide range of possible work could therefore be carried out on this process to optimize and characterize size-control and use the particles produced in various applications.

# Appendices

## Appendix A: Permeability data for Ag sample (data from Ralm Ricarte)

| Gas tested | Propylene | Propane | Ethylene | Ethane |
|---|---|---|---|---|
| Film thickness (cm) | 0.038 | 0.038 | 0.039 | 0.038 |
| Downstream volume ($cm^3$) | 334 | 332 | 334 | 332 |
| Film area ($cm^2$) | 2.19 | 2.19 | 2.19 | 2.19 |
| $\left(\frac{dp_1}{dt}\right)_{ss}$ At 172 kPa (cmHg/s) | $1.6x10^{-5}$ | $7.2x10^{-6}$ | $1.7x10^{-5}$ | $9.4x10^{-6}$ |
| $\left(\frac{dp_1}{dt}\right)_{ss}$ At 345 kPa (cmHg/s) | $2.8x10^{-5}$ | $1.1x10^{-5}$ | $2.7x10^{-5}$ | $1.6x10^{-5}$ |
| $\left(\frac{dp_1}{dt}\right)_{ss}$ At 517 kPa (cmHg/s) | $3.9x10^{-5}$ | $1.6x10^{-5}$ | $4.0x10^{-5}$ | $2.2x10^{-5}$ |
| $\left(\frac{dp_1}{dt}\right)_{ss}$ At 689 kPa (cmHg/s) | $5.5x10^{-5}$ | 2.2x10-5 | $4.9x10^{-5}$ | $2.6x10^{-5}$ |
| $\left(\frac{dp_1}{dt}\right)_{vac}$ (cmHg/s) | $8.5x10^{-7}$ | $7.9x10^{-7}$ | $1.8x10^{-6}$ | $1.3x10^{-6}$ |

## Appendix B: Permeability data for Au sample (data from Ralm Ricarte)

| Gas tested | Propylene | Propane | Ethylene | Ethane |
|---|---|---|---|---|
| Film thickness (cm) | 0.029 | 0.029 | 0.039 | 0.029 |
| Downstream volume ($cm^3$) | 334 | 331 | 334 | 331 |
| Film area ($cm^2$) | 2.19 | 2.19 | 2.19 | 2.19 |
| $\left(\frac{dp_1}{dt}\right)_{ss}$ At 172 kPa (cmHg/s) | $2.3x10^{-5}$ | $9.0x10^{-6}$ | $1.7x10^{-5}$ | $1.1x10^{-5}$ |
| $\left(\frac{dp_1}{dt}\right)_{ss}$ At 345 kPa (cmHg/s) | $3.4x10^{-5}$ | $1.4x10^{-5}$ | $2.7x10^{-5}$ | $1.8x10^{-5}$ |
| $\left(\frac{dp_1}{dt}\right)_{ss}$ At 517 kPa (cmHg/s) | $5.4x10^{-5}$ | $2.0x10^{-5}$ | $4.0x10^{-5}$ | $2.6x10^{-5}$ |
| $\left(\frac{dp_1}{dt}\right)_{ss}$ At 689 kPa (cmHg/s) | $7.8x10^{-5}$ | $2.7x10^{-5}$ | $5.0x10^{-5}$ | $3.5x10^{-5}$ |
| $\left(\frac{dp_1}{dt}\right)_{vac}$ (cmHg/s) | $3.0x10^{-6}$ | $3.0x10^{-6}$ | $1.8x10^{-6}$ | $6.5x10^{-7}$ |

# References


1. **Valden, M., Lai, X. and Goodman, D.W.** Onset of Catalytic Activity of Gold Clusters on Titania with the Appearance of Nonmetallic properties. *Science.* 1998, Vol. 281, pp. 1647-1650.

2. **Murray, C.B., Kagan, C.R. and Bawendi, M.G.** Synthesis and Characterization of Monodispersed Nanocrystals and Close-Packed Nanocrystal Assemblies. *Annual Review of Materials Science.* 2000, Vol. 30, pp. 545-610.

3. **Salata, O.V.** Applications of Nanoparticles in Biology and Medicine. *Journal of Nanobiotechnology.* 2004, Vol. 2.

4. **Roduner, E.** Size matters: why nanomaterials are different. *Chemical Society Reviews.* 2006, Vol. 35, pp. 583-592.

5. **Wang, Hai Tao, Lin, Dong Ming and Zhou, Xiao Ping.** Ethylene synthesis from the oxidative bromination of ethane. *Applied Catalysis.* 2009, 364, pp. 130-136.

6. **Staudt-Bickel, Claudia and Koros, William J.** Olefin/paraffin gas separations with 6FDA-based polyimide membranes. *Journal of Membrane Science.* 2000, Vol. 170, 2, pp. 205-214.

7. **Safarik, Douglas J. and Eldridge, R. Bruce.** Olefin/paraffin separations by reactive absorption: A review. *Industrial & Engineering Chemistry Research.* 1998, 37, pp. 2571-2581.

8. **Pinnau, I. and Toy, L.G.** Solid Polymer Electrolyte Composite Membranes for Olefin/Paraffin Separation. *Journal of Membrane Science.* 2001, Vol. 184, pp. 39-48.

9. **Kim, H.S., et al.** Reversible Olefin Complexation by Silver Ions in Dy Poly(vinyl methyl ketone) Membrane and its Application to Olefin/Paraffin Separation. *Chemical Communications.* 2000, pp. 1261-1262.

10. **Hong, S.U., et al.** Polymer-Salt Complexes Containing Silver Ions and Their Application to Facilitated Olefin Transport Membranes. *Advanced Materials.* 2000, Vol. 12, 13, pp. 968-971.

11. **Yoon, Y., Won, J. and Kang, Y.S.** Polymer Electrolyte Membranes Containing Silver Ion for Facilitated Olefin Transport. *Macromolecules.* 2000, Vol. 33, 9, pp. 3185-3186.

12. **Kang, Y.S., et al.** [ed.] Y. Yampolskii, I. Pinnau and B.D. Freeman. *Materials Science of Membranes for Gas and Vapor Separation.* s.l. : Wiley, 2006, 16, pp. 391-410.

13. **Hartley, F. R.** Thermodynamic Data for Olefin and Acetylene Complexes of Transition Metals. *Chemical Reviews.* 1973, Vol. 2, 73, pp. 163-189.

14. **Quinn, H.W., McIntyre, J.S. and Peterson, D.J.** Coordination Compounds of Olefins with Anhydrous Silver Salts. *Canadian Journal of Chemistry.* 1965, Vol. 43, 10, pp. 2896-2910.

15. **Morisato, A., et al.** Transport Properties of PA 12-PTMO/AgBFd Solid Polymer Electrolyte Membranes for Olefin/Paraffin Separation. *Desalination.* 2002, Vol. 145, pp. 347-351.

16. **Park, Y.S., Won, J. and Kang, Y.S.** Facilitated Transport of Olefin Through Solid PAAm and PAAm-graft Composite Membranes with Silver Ions. *Journal of Membrane Science.* 2001, Vol. 183, pp. 163-170.

17. **Lee, K.J., et al.** Complexation of Silver Ions with Poly(butylmethacrylate) and Propylene Toward Facilitated Propylene Transport. *Macromolecular Rapid Communications.* 2002, Vol. 23, 14, pp. 839-843.

18. **Kang, S.W., Char, K. and Kang, Y.S.** Novel Application of Partially Positively Charged Silver Nanoparticles for Facilitated Transport in Olefin/Paraffin Separation Membranes. *Chemistry of Materials.* 2008, Vol. 20, 4, pp. 1308-1311.

19. **Kang, S.W., et al.** Effect of the Polarity of Silver Nanoparticles Induced by Ionic Liquids on Facilitated Transport for the Separation of Propylene/Propane Mixtures. *Journal of Membrane Science.* 2008, Vol. 322, pp. 281-285.

20. **Kang, Y.S., et al.** Interaction with Olefins of the Partially Polarized Surface of Silver Nanoparticles Activated by p-Benzoquinone and Its Implications for Facilitated Olefin Transport. *Advanced Materials.* 2007, Vol. 19, pp. 475-479.

21. **Pozun, Z.D. and Henkelman, G.** A model to optimize the selectivity of gas separation in membranes. *Journal of Membrane Science.* 2010, Vol. 364, pp. 9-16.

22. **Pozun, Z.D., et al.** The Uniqueness of Silver for Olefin/Paraffin Separations. *Journal of Physical Chemistry.* 2011, Vol. 115, 5, pp. 1811-1818.

23. **Cao, G.** *Nanostructures and Nanomaterials, Synthesis, Properties and Applications.* s.l. : Imperial College Press, 2004. pp. 63-74.

24. **Pierre, A.C.** *Introduction to Sol-Gel Processing.* s.l. : Kluwer Academic Publishers, 1998.

25. **Becker, M.F., et al.** Metal nanoparticles generated by laser ablation. *Nanostructured Materials.* 1998, Vol. 10, 5, pp. 853-863.

26. **Lee, J., Becker, M. F. and Keto, J. W.** Dynamics of laser ablation of microparticles prior to nanoparticle generation. *Journal of Applied Physics.* 2001, Vol. 89, 12, pp. 8146-8152.

27. **Nichols, W. T.** *Production and Controlled Collection of Nanoparticles: Towards Manufacturing of Nanostructured Materials.* The University of Texas at Austin. 2002. Dissertation.

28. **Huang, C., et al.** Supersonic jet deposition of silver nanoparticle aerosols: Correlations of impact conditions and film morphologies. *Journal of Applied Physics.* 2007, Vol. 101, 064902.

29. **Henneke, D.E.** *Nanoparticles Produced Via Laser Ablation of Microparticles.* The University of Texas at Austin. 2001. Dissertation.

30. **Gallardo, I., Hoffman, K. and Keto, J.** Tuning the Absorption and Emission of CdSe and ZnS Core-Shell Nanoparticles by Laser Radiation . *SPIE.* 2008, Vol. 7030.

31. **Bohren, C.F. and Huffman, D.R.** *Absorption and Scattering of Light by Small Particles.* s.l. : Wiley, 1983.

32. **Marple, Virgil A. and Chien, Chung M.** Virtual Impactors: A Theoretical Study. *Environmental Science & Technology.* 1980, Vol. 14, 8, pp. 976-984.

33. **Chen, B.T., Yeh, H.C. and Cheng, Y.S.** A Novel Virtual Impactor: Calibration and Use. *Journal of Aerosol Science.* 1985, Vol. 16, 4, pp. 343-354.

34. **Chen, B.T. and Yeh, H.C.** An Improved Virtual Impactor: Design and Performance. *Journal of Aerosol Science.* 1987, Vol. 18, 2, pp. 203-214.

35. **Fuchs, N.A.** *The Mechanics of Aerosols.* New York : Pergamon Press, 1964. p. 154.

36. **Rader, Daniel J.** Momentum Slip Correction Factor for Small Particles in Nine Commmon Gases. *Journal of Aerosol Science.* 1990, Vol. 21, 2, pp. 161-168.

37. **Deslattes, R.D. and E.G. kessler, Jr.** [ed.] B. Crasemann. *Atomic Inner-Shell Physics.* New York : Plenum Press, 1985, pp. 181-235.

38. **Bearden, J.A.** X-Ray Wavelengths. *Reviews of Modern Physics.* 1967, Vol. 39, 1, pp. 79-124.

39. **Freeman, B.D. and Lin, H.** Permeation and Diffusion. [ed.] Czichos, Saito and Smith. *Handbook of Materials Measurement Methods.* s.l. : Springer, 2006, 7.6, pp. 371-386.

40. *Mathworks.* [Online] http://www.mathworks.com/help/toolbox/stats/lognpdf.html.

41. **Davis, C.E.** Student Works Sponsored by UT Faculty. *UT Digital Repository.* [Online] Aug. 2011. http://repositories.lib.utexas.edu/handle/2152/2.

42. **Emory, S.R., Haskins, W.E. and Nie, S.** Direct Observation of Size-Dependent Optical Enhancement in Single Metal Nanoparticles. *Journal of American Chemical Society.* 1998, 120, pp. 8009-8010.

43. **Nahar, M.** *Metal-on-oxide nanoparticles produced via laser ablation of microparticles.* The University of Texas at Austin. 2009. Thesis.

# Vita

Claire Elisabeth Davis was born on May 29th 1986 in Nantes, France. Claire pursued her education in Amiens and, in 2007, was accepted at Ecole Centrale de Lille for general engineering studies. This school gave her the opportunity to apply for graduate studies at The University of Texas at Austin. In 2009, Claire came to work at UT under supervision of Dr. Desiderio Kovar in the LAMA research group. She will graduate with a Master of Science in Materials Science and Engineering degree from UT Austin in August 2011 and with a Diplôme d'Ingénieur de L'Ecole Centrale de Lille in September 2011.

Permanent email addresses: claire.davis@utexas.edu or claire.davis@centraliens-lille.org

This Thesis was typed by: Claire Elisabeth Davis